Coastal Engineering 166 (2021) 103885

Contents lists available at ScienceDirect

Coastal Engineering

journal homepage: http://www.elsevier.com/locate/coastaleng

Modeling the hydrodynamics and morphodynamics of sandbar migration events

Yashar Rafati [a,*], Tian-Jian Hsu [a], Steve Elgar [b], Britt Raubenheimer [b], Ellen Quataert [c], Ap van Dongeren [c,d]

[a] Center for Applied Coastal Research, Department of Civil and Environmental Engineering, University of Delaware, Newark, DE, 19716, USA
[b] Woods Hole Oceanographic Institution, Woods Hole, MA, USA
[c] Department of Applied Morphodynamics, Deltares, Delft, the Netherlands
[d] Water Science and Engineering Department, IHE Delft, Delft, the Netherlands

ARTICLE INFO

Keywords:
XBeach
Cross-shore sediment transport
Roller energy
Wave skewness/asymmetry
Wave boundary layer streaming

ABSTRACT

A number of models are available for science and engineering purposes that numerically simulate nearshore hydrodynamics and the corresponding morphological evolution. However, the models include adjustable coefficients in parameterizations for physical processes that need to be calibrated, and thus there remains room for improvement by including additional physics. One such model is XBeach, which can simulate erosion during storms with proper calibration based on observations. The modeled sediment transport, especially in the cross-shore direction, is sensitive to the adjustable coefficients, with preferred values that are site and event specific. Here, the skill of XBeach is investigated by comparing 1-dimensional (cross-shore) depth-averaged simulations with observations of waves, currents, and sandbar migration across an Atlantic Ocean beach. Calibration of coefficients improved the agreement of the computed results with observed wave heights, offshore-directed mean currents (undertow), the wave-orbital-velocity third moments (skewness and asymmetry), and onshore/offshore sandbar migration although the proposed coefficient values depend on the parameterizations used. For example, including a variable breaking-wave roller energy model resulted in more skillful predictions of undertow than using the default constant coefficient value. Using the calibrated roller coefficients and corresponding undertow, XBeach simulated the observed offshore migration of the sandbar. Onshore transport in XBeach is driven by non-sinusoidal wave-orbital velocities, and proposed values for coefficients depend on the parameterization used to estimate skewness and asymmetry and the associated transport, as well as on incident wave conditions. XBeach calculations of cross-shore sediment transport rates were compared with those estimated by a commonly used sediment transport formula based on laboratory experiments. The inter-comparison suggests that using a wave-induced onshore transport parameter 3 or 4 times larger than the default value may at least in part compensate for the lack of bottom-boundary-layer-streaming-driven-onshore transport in XBeach.

1. Introduction

Understanding coastal morphological changes during storms and the subsequent recovery is crucial to coastal management. Physics-based numerical models are a useful tool to predict the coupled hydrodynamic-morphodynamic processes in the nearshore. Models that simulate processes on the time scale of individual waves (phase-resolving models, Shi et al., 2012; Zijlema et al., 2011) have skill in shallow water, but are computationally expensive, and currently are limited to simulating only the hydrodynamics without the morphodynamics. In contrast, models that simulate processes by averaging over many wave periods (phase-averaged models, Lesser et al., 2004; Warner et al., 2010) are significantly less expensive computationally than phase-resolving models. The tradeoff for computational efficiency is that phase-averaged models parameterize many processes, such as wave breaking, the rollers of white foam on the front face of breaking waves, and aspects of the mechanics of sediment transport. XBeach-Surfbeat (XB-SB) is a commonly-used model that is in between phase-averaging and phase-resolving models, and resolves the amplitude variation on the time scale of wave groups (Roelvink et al., 2009).

* Corresponding author.
E-mail address: yashar@udel.edu (Y. Rafati).

https://doi.org/10.1016/j.coastaleng.2021.103885
Received 11 October 2020; Received in revised form 5 February 2021; Accepted 6 March 2021
Available online 10 March 2021

XB-SB has been used to predict storm-induced beach erosion (Kalligeris et al., 2020), dune erosion (Berard et al., 2017; Elsayed and Oumeraci, 2017; Splinter and Palmsten, 2012), overwash, breaching, and inundation (de Vet et al., 2015; Passeri et al., 2018; Schweiger et al., 2020; Van der Lugt et al., 2019; Vousdoukas et al., 2012), as well as beach recovery (Roelvink and Costas, 2019).

The hydrodynamic drivers of sediment transport in XB-SB are the mean currents, the parameterized breaking wave turbulence, and the parameterized third moments (skewness and asymmetry) of the near-bed wave-orbital velocity. There has been a great deal of effort to calibrate the parameters used in XB-SB to predict the beach morphological response under different offshore wave energy conditions (Berard et al., 2017; Elsayed and Oumeraci, 2017; Schambach et al., 2018; Splinter and Palmsten, 2012; Vousdoukas et al., 2012). However, the model coefficients that produce the most skillful predictions of observed bathymetric change often are site-specific. For example, calibration on three adjacent beaches in southeast Australia under different storm conditions suggested different values both for the wave breaker index and for an empirical coefficient associated with onshore transport for each site (Simmons et al., 2019). Furthermore, at a site with a specific set of model parameters, the model performance predicting the morphological changes was event dependent. As an example, model simulations of the morphological change observed on Dauphin Island, AL using the same calibration factors were significantly more skillful during Hurricane Katrina than during Hurricane Ivan (Passeri et al., 2018).

The range of the calibrated model parameters in sediment transport formulations used in XB-SB has been attributed to unresolved physical processes (Kalligeris et al., 2020; Nederhoff, 2014). Using a spatially varying dynamic roughness in the subaerial region can compensate for some unresolved physics, resulting in a more skillful prediction of overwash and breaching during hurricanes (Van der Lugt et al., 2019). The main objective here is to evaluate different physics included in the hydrodynamics and sediment transport parameterizations of XB-SB. The focus is on simulating nearshore sandbar migration, which occurs in an area of the surf zone for which the hydrodynamics are relatively well-understood, and for which there are significant in situ observations for the data set investigated here, unlike in the swash zone and dune region.

Surf zone sandbars are important morphological features that protect sandy beaches by dissipating incoming wave energy before it reaches the shoreline. Sandbars have a much larger-scale (longer) spatial (temporal) variability than the individual waves. During storms, waves break on the sandbar, driving an offshore-directed mean current (undertow) that balances the onshore mass flux near the surface of the breaking waves, including a contribution from the wave roller energy in the breaking region (Garcez Faria et al., 2000; Svendsen, 1984a). Undertow tends to be largest between the shoreward slope of the sandbar and the bar crest, and thus its cross-shore gradients transport sediment seaward, and the sandbar migrates offshore (Gallagher et al., 1998; Masselink et al., 2016; Thornton et al., 1996). In contrast to the offshore bar migration during energetic waves, sandbars migrate onshore during moderate and small waves (Elgar et al., 2001; Hoefel and Elgar, 2003; Hsu et al., 2006). Under these conditions, undertow is relatively weak, and asymmetrical wave-orbital velocities mobilize sediment and transport it shoreward. In general, both undertow and asymmetrical velocities occur simultaneously, and bar migration is a balance between the corresponding offshore and onshore sediment transport fluxes (Hsu et al., 2006; Ruessink et al., 2016). Sandbars also control the location of the wave breaking, which provides the main forcing for the alongshore current (Ribas et al., 2011; Thornton and Kim, 1993). Here, the focus is on cross-shore processes during bar-migration events when the bathymetry is mostly alongshore uniform and the alongshore gradients in alongshore currents and sediment transport are small (Gallagher et al., 1998).

Asymmetrical wave-orbital velocities can be characterized statistically by the third moments of the time series, referred to as skewness and asymmetry (Elgar and Guza, 1985). As waves shoal, they become skewed with sharp crests and broad, flat troughs. If sediment is transported by an odd power of the velocity, more sediment is transported shoreward under the high-velocity sharp peaks than seaward under the slower-velocity, flat troughs (Hsu and Hanes, 2004; O'Donoghue and Wright, 2004; Ribberink and Al-Salem, 1994). In shallower water, the waves pitch forward, with steep front faces and more gently sloping rear faces (sawtooth-like or asymmetrical shape). Thus, the wave-orbital velocity is asymmetric and the wave-orbital acceleration time series is skewed (Elgar et al., 1988), which causes more sediment to be transported under the strong shoreward accelerations as the steep front face passes than transported under the weaker seaward accelerations under the gently sloping rear face of the wave (Drake and Calantoni, 2001; Hoefel and Elgar, 2003; Hsu and Hanes, 2004; Van der A et al., 2010). Progressive wave boundary layer streaming also can lead to onshore sediment transport and sandbar migration (Henderson et al., 2004; Kim et al., 2018; Kranenburg et al., 2013). Here, special attention is paid to the effectiveness of the third moments and wave streaming on driving onshore sediment transport, and how XB-SB calibration can compensate for the streaming effect that is absent in XB-SB.

Offshore sandbar migration observed during high-energy incident waves on an Atlantic Ocean beach near Duck, NC was simulated accurately using the energetics sediment transport formula of Bailard (1981) forced by the velocities recorded at current meters (Gallagher et al., 1998; Thornton et al., 1996). However, the onshore bar migration observed during low-energy conditions was not reproduced. By modifying the energetics approach including transport driven by skewed wave-orbital accelerations (Drake and Calantoni, 2001), the observed onshore sandbar migration was simulated accurately (Hoefel and Elgar, 2003). With certain parameterizations of wave-current interaction in the energetics model, velocity skewness could contribute to onshore sandbar migration (Hsu et al., 2006). Both onshore and offshore sandbar migration were predicted by incorporating velocity and acceleration skewness (Dubarbier et al., 2015; Fernández-Mora et al., 2015; Wenneker et al., 2011). Most of these studies were based on phase-resolving analysis and therefore their applicability to phase-averaged morphodynamic models faces several challenges.

Third moments in phase-averaged models such as XB-SB are often parameterized based on local properties of the waves and bathymetry. Comparisons of observed third moments with the parameterized values have significant scatter, even among the observations for which the parameters were developed (Doering and Bowen, 1995; Rocha et al., 2017; Ruessink et al., 2012; Van Thiel De Vries, 2009). In this study, the latter two parameterizations are tested for low- and high-energy conditions, and model coefficients are calibrated to obtain the best agreement with the measured morphology changes in the sandbar region.

Here, the skill of XB-SB predicting observed hydrodynamics is evaluated, and the model sediment transport parameters during onshore and offshore sandbar migration events are calibrated to provide the best predictions of the morphodynamic evolution. Comparisons with observations suggest that given a proper calibration of the model coefficients, XB-SB can simulate fairly accurately the observed near-bed wave-orbital velocity magnitudes, undertow currents, and third moments in the shoaling region and surf zone. The model results suggest a modification to the wave roller energy formulation that improves undertow predictions during energetic waves. In addition, XB-SB predictions of wave-induced sediment fluxes in the sandbar region are compared with those calculated by a commonly used formula that was developed based on laboratory experiments of wave-induced sediment transport (Van der A et al., 2013), providing some insight into how tuning parameters in the XB-SB sediment transport formulation can compensate for some unresolved physics.

2. Model description

The XBeach-Surfbeat (Roelvink et al., 2009) solves the nonlinear shallow water equations for the mean flows with the wave forcing

provided by solving the wave-action and wave-roller energy equations. The sediment transport model solves an advection-diffusion equation for the depth-averaged concentration, where the contribution of the wave nonlinearity is included as an advection term in the equation. The bed morphology evolution is then calculated by employing Exner's equation. Some details of the cross-shore terms in the momentum and advection-diffusion equations implemented in the model are presented here (subsections 2.1 and 2.2), with more information about the model formulation provided in the recent version of the XBeach manual (Hoonhout, 2018) and in the Appendix.

2.1. Surface rollers

Although waves may break in a specific location (e.g., on the sandbar crest), momentum is not transferred instantly to the water column and seafloor. Instead, mass and momentum are carried shoreward by surface rollers (the air-water mixture on the surface of breaking waves) on the front face of the waves (Svendsen, 1984b). The shoreward flux of mass and momentum results in an offshore-directed return flow (undertow) beneath the wave troughs (Garcez Faria et al., 2000; Svendsen, 1984a). The roller energy is calculated in XB-SB with,

$$\frac{\partial E_r}{\partial t}+\frac{\partial c_x E_r}{\partial x}+\frac{\partial c_y E_r}{\partial y}+\frac{\partial c_\phi E_r}{\partial \phi}=D_w-D_r, \tag{1}$$

where $E_r(x,y,t,\phi)$ is the roller energy in each directional bin as a function of cross- (x) and alongshore (y) coordinate, time (t) and the angle of incidence with respect to the x-axis (ϕ), c_x, c_y, and c_ϕ are the wave celerities in the x, y, and ϕ direction, respectively, and the source term D_w is given by the wave-breaking-induced dissipation. The roller energy dissipation term D_r is quantified by the shear stress applied from the roller to the fluid underneath, and is given by:

$$D_r=2\beta\frac{g}{c_g}E_r, \tag{2}$$

where β is a coefficient with the default value of 0.1, g is gravitational acceleration, and c_g is the wave group velocity. Based on numerical experiments, the β coefficient affects the strength of the undertow (Garcez Faria et al., 2000), which is discussed in more detail in Section 3.3. The radiation stresses $S_{ij,r}(x,y,t)$ induced by the roller (source terms in Eqns. AA.1 and AA.2, Appendix A.1) is obtained by integrating the roller energy over the directional bins,

$$S_{xx,r}(x,y,t)=\int cos^2\phi E_r d\phi, \tag{3}$$

$$S_{xy,r}(x,y,t)=S_{yx,r}=\int sin\phi cos\phi E_r d\phi, \tag{4}$$

$$S_{yy,r}(x,y,t)=\int sin^2\phi E_r d\phi. \tag{5}$$

2.2. Sediment transport

The advection-diffusion equation used in the sediment transport formulation (Eqn (AA.11), Appendix A.3) includes an advective-velocity term (u_a) to account for third moments of orbital velocities (skewness and asymmetry). The advective-velocity term depends on the strengths of the wave-orbital velocity skewness and asymmetry, which are adjusted with a coefficient γ_{ua}, such that the advective-velocity coefficient u_a is given by,

$$u_a=(S_k-A_s)\gamma_{ua}u_{rms}, \tag{6}$$

where S_k is skewness, A_s is asymmetry, and u_{rms} is the root-mean-square orbital velocity (see Appendix A.3 and A.4).

To avoid excessive erosion near the shoreline, sediment flux in the swash zone, q_{swash} is adjusted with an empirical correction (Roelvink and Costas, 2017):

$$q_{swash}=q-f_{swash}|q|\left(\frac{\partial z_b}{\partial x}-S_{berm}\right),\ for\quad \frac{H_{rms}}{h}>\gamma_{berm} \tag{7}$$

where q is the sediment flux, f_{swash} is a transport factor, z_b is the bed elevation, S_{berm} is the berm slope (near the shoreline), and γ_{berm} is the lower limit ratio of root-mean-square wave height H_{rms} to water depth h. Here, $f_{swash}=30$, $S_{berm}=0.1$, and $\gamma_{berm}=0.7$ are used.

XB-SB includes two parameterizations for wave skewness and asymmetry. In one form, skewness and asymmetry are calculated from a time series of velocity based on stream function theory (Rienecker and Fenton, 1981) using a non-dimensional wave period ($T_{rep}\sqrt{g/h}$) and wave height (H_{rms}/h) (Van Thiel De Vries 2009). This formulation has a parameter that describes the wave shape, ranging from skewed (Stokes waves) to asymmetric (sawtooth waves) (see Appendix A.4), and provides an estimate of the period of broken-wave bores, T_{bore}, used in estimation of near-bed turbulence (Appendix A.3).

An alternative approach to parameterizing third moments is based on the local Ursell number (Ruessink et al., 2012), given by

$$Ur=\frac{3\sqrt{2}}{8}\frac{H_{rms}k}{(kh)^3}, \tag{8}$$

where k is the wavenumber corresponding to the centroid of the frequency spectrum (wind-wave frequency (f) band, $0.04<f<0.50$ Hz). Details of the wave-shape parameterizations are in Appendix A.4. The fit to the Ursell number parameterization was based on a range of field observations, many of which were obtained at the same site as the data discussed here (see Fig. 5 of Ruessink et al., 2012).

XB-SB incorporates the effect of wave-breaking-induced turbulence on sediment entrainment by estimating near-bed wave-breaking turbulence using either a "wave-averaged" or "bore-averaged" (Eqns. (AA.17) and (AA.18), Appendix A.3) formulation. In the current version of XB-SB, the bore-averaged formulation of near-bed turbulence k_b (Appendix A.3) can be used only with the stream-function parameterization of third moments (Van Thiel De Vries, 2009; Appendix A.4). Thus, to investigate how the wave-shape parameterizations affect sediment transport and sandbar migration, the XB-SB source code was modified such that here the bore-averaged turbulence model can be implemented with both parameterizations for third moments.

3. Model-data comparisons

3.1. Field observations

Water levels, waves, currents (sampled at 2 Hz), and bathymetry (measured nearly daily) were observed along a transect extending from the shoreline to 8-m water depth during September and October 1994 at the US Army Corps of Engineers Field Research Facility, near Duck, NC (http://frf.usace.army.mil/frf.shtml) (Fig. 1) (Gallagher et al., 1998). The current meters were located between 0.4 and 1.0 m above the seabed. To smooth the small alongshore variability in the bathymetry, between 4 and 9 cross-shore surveys ±100 m from the instrumented transect were averaged to produce the bathymetry used in one-dimensional (cross-shore) model simulations. The spacing between the surveyed cross-shore transects varied daily owing to conditions (~20–40 m).

One onshore and three offshore sandbar migration events were observed. The ~20-m onshore bar migration (Event II, Fig. 2b) had relatively small incident waves after the first day. The offshore migration events occurred during energetic incident waves (Events I, III, and IV, Fig. 2a,c,d). The start and end dates for events II, III, and IV are altered slightly from those reported previously (Gallagher et al., 1998) to use spatially dense surveyed cross-shore profiles (not performed every

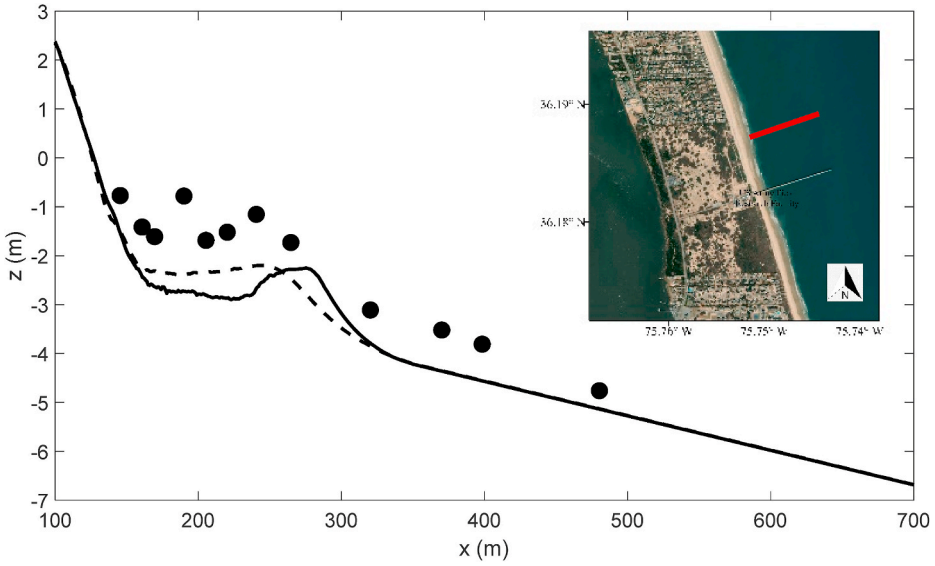

Fig. 1. Seafloor elevation (z, relative to NAVD88) versus cross-shore location x observed on September 7 (dashed curve) and October 14 (solid curve) 1994 at the USACE Field Research Facility on the Outer Banks, near Duck, NC (inset). The symbols are locations of colocated pressure gauges and current meters. The instrumented transect is indicated by the red line in the inset Google Earth image. (For interpretation of the references to colour in this figure legend, the reader is referred to the Web version of this article.)

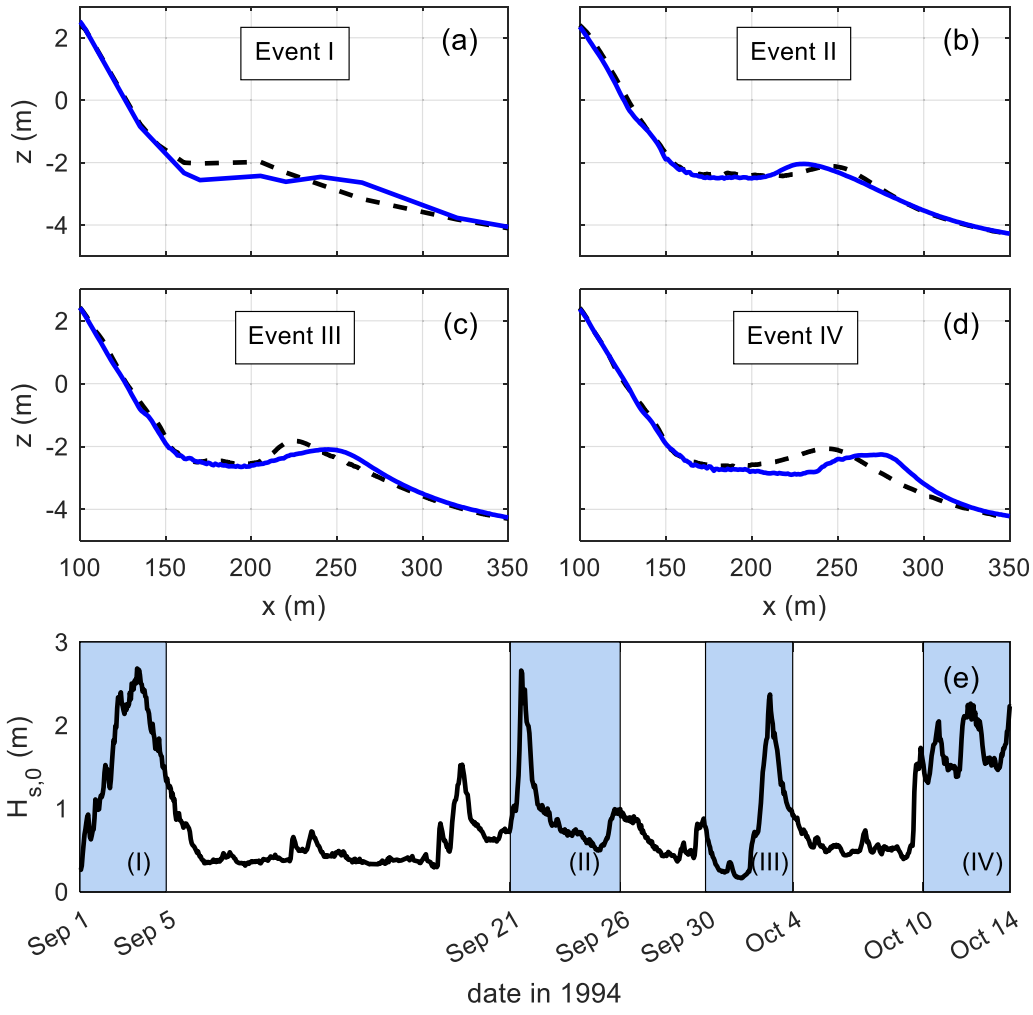

Fig. 2. Seafloor elevation z versus cross-shore location x for (a) Event I (offshore sandbar migration between September 1 (dashed-black curve) and September 5 (solid-blue curve)), (b) Event II (onshore migration between September 21 (dashed-black) and September 26 (solid-blue)), (c) Event III (offshore migration between September 30 (dashed-black) and October 4 (solid-blue)), and (d) Event IV (offshore migration between October 10 (dashed-black) and October 14 (solid-blue)), and (e) hourly averaged significant wave height measured in 8-m water depth $H_{s,0}$ versus date (sandbar migration event dates shaded in blue). (For interpretation of the references to colour in this figure legend, the reader is referred to the Web version of this article.)

day), rather than spatially-sparse estimates of the sandbar location from the 10 fixed altimeters (every 3 h). Thus, the simulations of the onshore migration Event II started on September 21 (nearest date of a survey), which included incident waves ~2-m high that may have caused some offshore migration before the waves decreased and onshore migration began (Fig. 2e). For Event I (Fig. 2a), there were no surveys near the start and end dates, and thus the bed-level data from fixed altimeters were used to generate the initial and final profiles without alongshore averaging. The onshore migration Event II and the offshore migration Event IV were used to calibrate the model coefficients. The other two offshore migration events (I and III) were used to test the calibrated coefficients.

3.2. Model setup

One-dimensional (1D) XB-SB simulations were initialized with the cross-shore bathymetry described above. During the four sandbar migration events studied here, morphological changes in the alongshore were much smaller than those in the cross-shore and alongshore gradients did not contribute significantly to the observed morphological evolution (Gallagher et al., 1998), consistent with many modeling studies of the sandbar migration on this data set (Dubarbier et al., 2015; Elgar et al., 2001; Fernández-Mora et al., 2015; Gallagher et al., 1998; Henderson et al., 2004; Hsu et al., 2006).

The model grid size varied in the cross-shore direction from 5-m spacing in shallow water ($h < 2$ m) to about 15-m spacing at the offshore boundary (~8-m water depth). Model results using 1- and 2-m grid spacing are not significantly different than those using 5-m spacing, consistent with previous XB-SB simulations at Duck, NC (Roelvink et al, 2009, 2018). The total number of grid cells ranged from 106 to 134 for different simulation cases. $d_{50} = 0.2$ mm (median grain diameter) was used in the simulations presented here consistent with the samples in the sandbar region sediment indicating $d_{50} \sim 0.2$ mm (Gallagher et al., 1998). Sensitivity tests suggest that model results do not change significantly for $0.15 < d_{50} < 0.30$ mm. Model results were not sensitive to morphological acceleration factors ("morfac", Ranasinghe et al., 2011) from 1 to 10, and thus the more computationally efficient morfac = 10 was used, consistent with previous studies (Harter and Figlus, 2017; Pender and Karunarathna, 2013; Vousdoukas et al., 2012). Forcing at the offshore boundary was based on the hourly-averaged tidal levels and wave heights, periods, and directions estimated from observations in 8 m depth.

Here, the focus is on the model sensitivity to the coefficients that control the roller energy dissipation (β) and the role of third moments on the sediment fluxes (γ_{ua}), with and without the empirical shoreline slope correction (Table 1). The sensitivity to parameters in the sub-model formulations (e.g., bed friction, aspects of wave breaking) was also investigated, and the values that resulted in the highest model skill are used here (Table AA.1, Appendix). All other model coefficients use the default values.

Table 1
XB-SB model runs (Setup ID) and associated coefficients γ_{ua} and β, wave-shape model, and whether or not the berm slope (BS) correction was applied.

Setup ID	β	γ_{ua}	Wave-shape model	BS[a]
VT09_I (default)	0.1	0.1	Van Thiel De Vries (2009)	off
VT09_II	f (k, h, H_{rms})	0.1		off
VT09_III	f (k, h, H_{rms})	0.3		off
VT09_IV	f (k, h, H_{rms})	0.35		off
VT09_V	f (k, h, H_{rms})	0.4		off
VT09_VI	f (k, h, H_{rms})	0.3		on
VT09_VII	f (k, h, H_{rms})	0.35		on
R12_I	0.1	0.1	Ruessink et al. (2012)	off
R12_II	f (k, h, H_{rms})	0.1		off
R12_III	f (k, h, H_{rms})	0.3		off
R12_IV	f (k, h, H_{rms})	0.4		off
R12_V	f (k, h, H_{rms})	0.55		off
R12_VI	f (k, h, H_{rms})	0.4		on
R12_VII	f (k, h, H_{rms})	0.55		on

[a] "BS" refers to the berm slope correction (Eqn. (7)).

3.3. Simulations of hydrodynamics

The capability of the XB-SB model to predict the cross-shore variations of wave height, undertow current, wave-orbital velocity, and wave skewness and asymmetry was investigated by simulating specific 1-h intervals during the onshore and offshore bar migration events, each with different incident wave conditions (Table 2).

Using the default input parameters (VT09_I in Table 1, blue curves in Fig. 3), the model simulates the observed wave heights along the cross-shore transect in both events accurately (Fig. 3c and d). For the high-energy conditions, the simulated wave heights are slightly higher than observed onshore of the sandbar (Fig. 3c). However, using the default coefficients during high-energy incident waves, XB-SB significantly under-predicts the undertow near and onshore of the sandbar (Fig. 3e). Undertow is driven by radiation stresses, which are affected by roller energy dissipation (Eqn. (2)). Wave-breaking dissipation is the source term in the roller energy balance (Eqn. (1)), and thus during energetic incident waves, high roller energy is generated in the bar region where wave breaking is significant (Fig. 3g), in contrast with the much smaller roller energy during less energetic waves (Fig. 3h). Sensitivity analysis of different model coefficients in XB-SB, including coefficients corresponding to the wave breaking dissipation and bottom friction, suggested that the under-prediction of undertow is most likely due to under-prediction of the roller energy E_r.

Parameterization of the roller dissipation rate (D_r, Eqn. (2)), which is a sink term in the roller energy balance equation, was found to be effective in controlling the roller energy, and thus in the resulting undertow. Decreasing the roller dissipation coefficient β from the default value of 0.1 reduces the roller dissipation rate, leading to a higher roller energy (E_r) and a larger undertow current. To compensate for the underprediction of undertow in the breaking region, a different formulation of β based on the local wave height, wave number, and water depth is used (Walstra et al., 1996):

$$\beta = \beta_1 kh \frac{h - H_{rms}}{H_{rms}} < 0.1, \tag{9}$$

where β_1 is a tuning coefficient. Here, a slight modification that yielded better simulations of undertow in the inner surf zone is used. Specifically, in the modified formulation $\beta_1 = 0.03$ and a limiter is included that allows β to approach the default value and maintain the roller dissipation in the swash zone:

$$\beta = \begin{cases} 0.03kh\dfrac{h - H_{rms}}{H_{rms}} < 0.1 \\ 0.1\ , \ kh < 0.45 \end{cases}, \ kh > 0.45 \tag{10}$$

The cross-shore variations of β, the roller energy (E_r), and the roller

Table 2
Incident (8-m water depth) wave characteristics for the 1-h hydrodynamic simulations, with $H_{s,0}$ the significant wave height, T the centroidal period, θ the angle (degrees) of the waves relative to shore normal (positive values represent waves coming from north-east), and the tide level (relative to NAVD88) for categories of high or low incident wave energy.

	Category	$H_{s,0}$ (m)	T (s)	θ	Tide level (m)
September 4, 12:00 to 13:00 EST	High-energy	2.68	6.45	8.4	−0.59
September 24, 12:00 to 13:00 EST	Low-energy	0.70	7.96	−9.4	0.16
October 3, 13:00 to 14:00 EST	High-energy	2.37	5.84	16.4	−0.36
October 12, 10:00 to 11:00 EST	High-energy	2.07	6.01	10.6	0.04

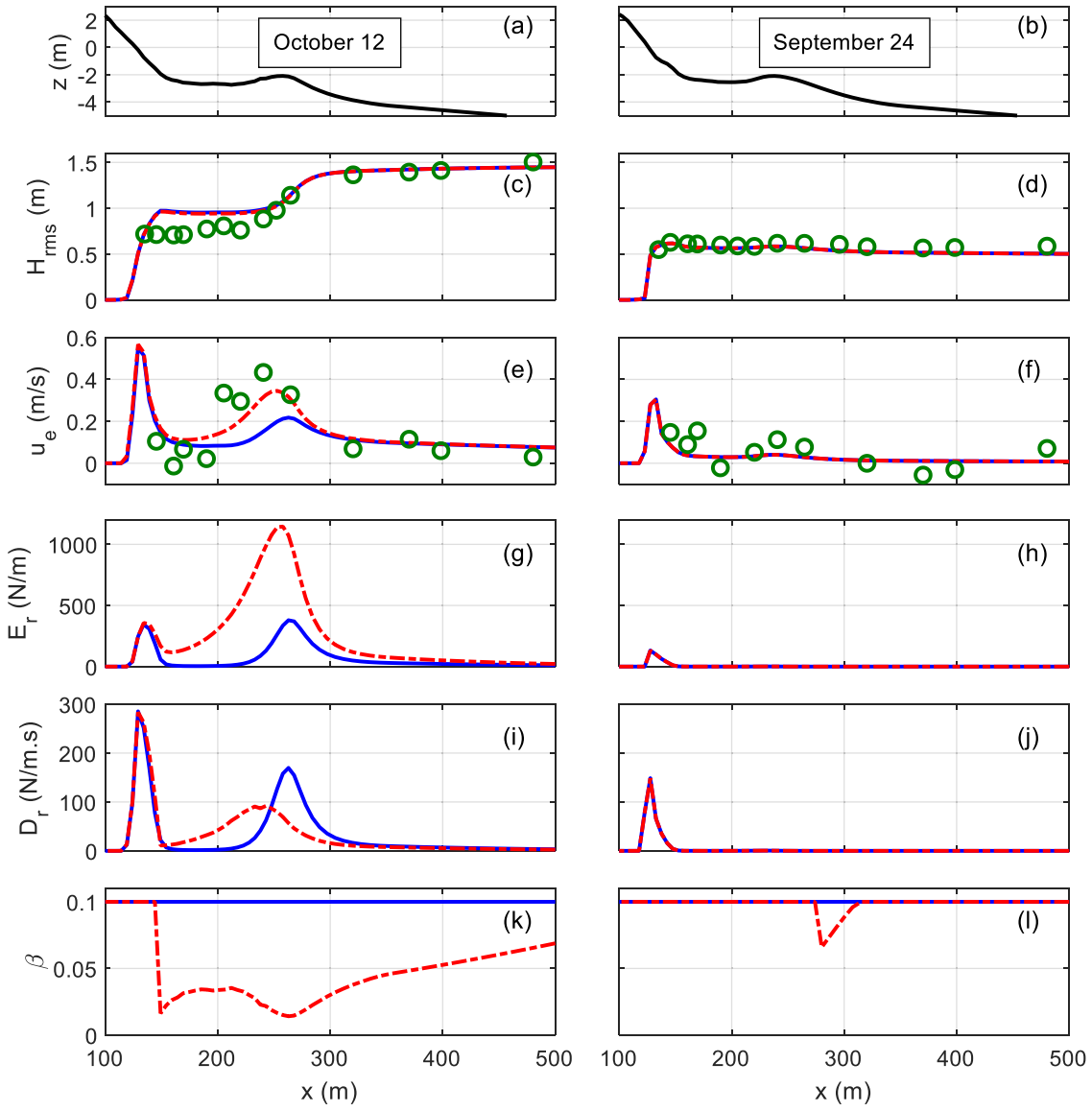

Fig. 3. (a, b) Seafloor elevation z, (c,d) root-mean-square wave height H_{rms}, (e,f) mean offshore-directed current (undertow) u_e, (g,h) roller energy E_r and (i,j) roller dissipation rate D_r integrated over all directional bins, and (k,l) roller dissipation coefficient β versus cross-shore location for (left side, a,c,e,g,i,k) Event IV (October 12, $H_{s,0} = 2.07$ m ($H_{rms,0} = 1.46$ m)) and (right side, b,d,f,h,j,l) Event II (September 24, $H_{s,0} = 0.70$ m ($H_{rms,0} = 0.49$ m)). The green symbols are observations, and the curves are for XB-SB using default parameters (VT09_I, solid-blue curves) and using variable β (VT09_II, red-dashed curves). (For interpretation of the references to colour in this figure legend, the reader is referred to the Web version of this article.)

energy dissipation rate (D_r) during energetic waves are affected significantly by the different approaches to rollers (compare blue with dashed-red curves in Fig. 3g,i,k), whereas during low-energy conditions, the two approaches are similar (Fig. 3h,j,l). Using the new formulation, β reduces to a value as low as $\beta = 0.01$ near the bar region compared with the default value of $\beta = 0.1$ (Fig. 3k). Accordingly, using the variable β formulation, a lower roller dissipation rate (Fig. 3i) is obtained at the bar crest, resulting in significantly higher roller energy (Fig. 3g) and undertow intensity (Fig. 3e) at the bar crest. Overall, using the variable β formulation causes less dissipation of the roller energy in the bar region, resulting in higher radiation stress induced by roller energy that generates stronger undertow. During low-energy waves, the new formulation of roller dissipation does not affect the calculated undertow or roller energy (Fig. 3f,h), because wave breaking near the bar location is not significant (Fig. 3d), and thus the roller does not contribute to the undertow.

XB-SB predictions of the cross-shore variations of wave height and undertow also were evaluated for the other two high-energy events of October 3 and September 4 (Fig. 4). Using the variable β formulation, the model simulates the observed wave heights accurately (Fig. 4c and d), and the undertow fairly well (Fig. 4e and f), especially near the sandbar. Model performance near the sandbar ($200 < x < 350$ m) is evaluated with the relative mean absolute error (RMAE (Van Rijn et al., 2003)) (Table 3). Using the new formulation of β to control the roller dissipation, the model performance in predicting the undertow during high-energy conditions (Table 3, September 4, October 3, and October 12) improved significantly compared with a fixed value of β (RMAE decreased by 25%–50%), although the skill of simulating wave heights is not affected (RMAE between 0.07 and 0.20).

The model sediment transport formulations are driven by wave skewness (S_k), asymmetry (A_s), the wave-orbital velocity (u_{rms}), and the mean velocity (Appendix A.3). Using time series of observed cross-shore velocities u, wave skewness and asymmetry are calculated as (Elgar and Guza, 1985),

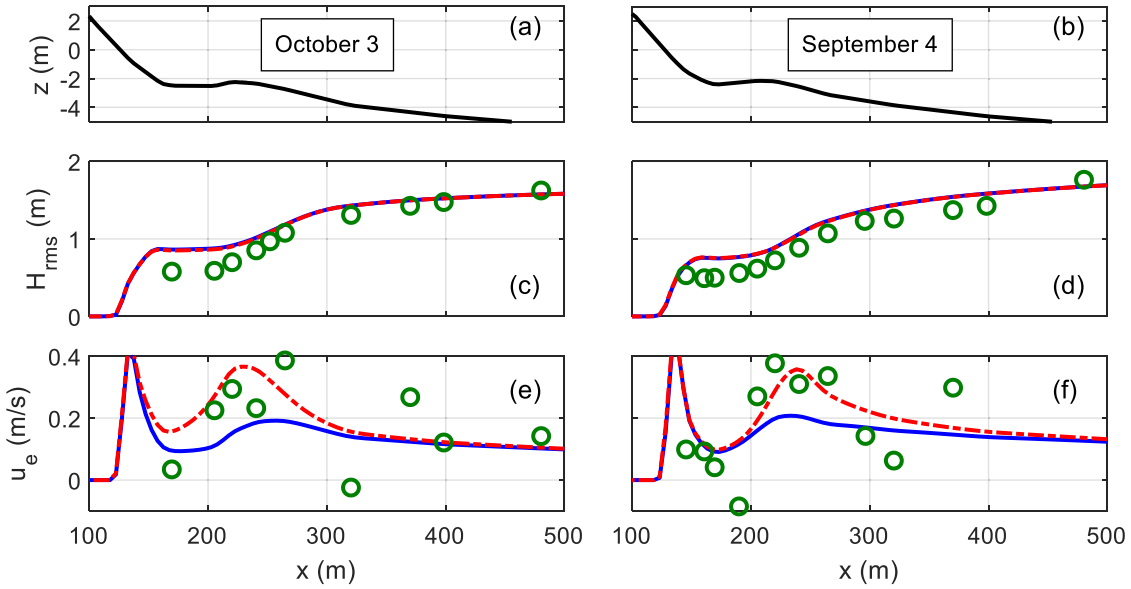

Fig. 4. (a,b) Seafloor elevation z, (c,d) root-mean-square wave height H_{rms}, and (e,f) mean offshore-directed current (undertow) u_e, versus cross-shore location for (left side, a,c,e) Event III (October 3, $H_{s,0} = 2.37$ m ($H_{rms,0} = 1.68$ m)) and (right side, b,d,f) Event I (September 4, $H_{s,0} = 2.68$ m ($H_{rms,0} = 1.89$ m)). The green symbols are observations, and the curves are for XB-SB using default parameters (VT09_I, solid-blue curves) and using variable β (VT09_II, red-dashed curves). (For interpretation of the references to colour in this figure legend, the reader is referred to the Web version of this article.)

$$S_k = \frac{\langle u^3 \rangle}{\langle u^2 \rangle^{3/2}} \tag{11}$$

and

$$A_s = \frac{\langle H(u)^3 \rangle}{\langle H(u)^2 \rangle^{3/2}} \tag{12}$$

where $H(u)$ is the Hilbert transform of the velocity time series, and the angle brackets denote time averaging.

The model predictions of the wave-orbital velocity are accurate (Fig. 5c,d,i,j) (RMAE between 0.09 and 0.35, Table 3) for all four events. During high-energy events (September 4, October 3, and October 12), both wave-shape parameterizations (Ruessink et al., 2012 and Van Thiel De Vries, 2009) result in fairly accurate predictions of the observed asymmetry (Fig. 5e,k,l, compare dashed curves with each other and with the triangles). Measured wave skewness during high-energy conditions does not have significant cross-shore variability (green circles in Fig. 5e, k,l), and the Ruessink et al. (2012) wave-shape parameterization (solid-red curves in Fig. 5e,k,l) is more skillful than Van Thiel De Vries (2009) (solid-blue curves in Fig. 5e,k,l), which over-predicts the wave skewness both in the bar region and near the berm. During low-energy condition, there was limited wave breaking on the sandbar and in the trough between the bar and the shoreline (Fig. 3d), and the observed skewness increased shoreward from the crest of the sandbar, reaching its highest value in the bar trough (Fig. 5f) before there is significant wave breaking (Dibajnia et al., 2001; Rocha et al., 2017). The observed evolution of skewness is not predicted by either parameterization (solid curves in Fig. 5f). Similarly, during low-energy condition, both parameterizations underpredict asymmetry near the bar crest by 30%–45%, and overpredict asymmetry onshore of the sandbar (Fig. 5f, compare the dashed curves with the green triangles).

3.4. Simulation of sandbar migration

The variable roller dissipation coefficient β (Eqn. (10)) implemented here in XB-SB and the two forms for third-moment parameterizations previously implemented in XB-SB were used to investigate the model skill simulating the observed sandbar migration events. The best sediment transport parameter γ_{ua} for each model was determined by varying γ_{ua} in increments of 0.05 above the default value of $\gamma_{ua} = 0.1$ and calculating the corresponding model skill simulating observed onshore (Event II, Fig. 2b) and offshore (Event IV, Fig. 2d) sandbar migration events. Simulation results are presented for the default value of $\gamma_{ua} = 0.1$ and for the best values of γ_{ua} (Figs. 6 and 7). Using the tuned parameters, model simulations were compared with the other two observed offshore bar migration events (Event I, Fig. 2a and Event III, Fig. 2c). Model performance predicting the morphodynamics is evaluated with the Brier Skill Score (BSS) and the root mean square error (RMSE) between simulated and observed seafloor elevation change (Tables 4 and 5). The comparisons have been divided into the region between the shoreline and the trough (depression) in the bathymetry onshore of the sandbar ($100 < x < 200$ m) and the region that encompasses the sandbar ($200 < x < 350$ m). The rate of observed morphological change was relatively small in the shallower region, and thus only RMSE was calculated (Table 5).

Model results were compared with observations during offshore bar migration Event IV for different parameterizations of third moments, different approaches to estimating β, and different values of the tuning coefficient γ_{ua} that establishes the strength of the third moments in the sediment transport formulation (Fig. 6). Using the default values for the input parameters ($\beta = 0.1$ and $\gamma_{ua} = 0.1$), neither third-moment formulation predicts the observed offshore sandbar migration (Fig. 6a and b, Table 4, VT09_I and R12_I), consistent with XBeach simulations of beach profiles in Southern California under moderate storms where the observed offshore sandbar formation was not simulated (Kalligeris et al., 2020). Using a variable β in the roller formulation (Eqn. (10)), XB-SB predicts the relatively strong undertow observed near the bar crest (Fig. 3e) and the corresponding offshore bar migration (similar to Gallagher et al., 1998; Thornton et al., 1996) using either third-moment parameterization, although the simulated bar crest is lower and farther offshore than observed (Fig. 6c and d, Table 4, VT09_II and R12_II). Furthermore, both models predict significant erosion near the shoreline (Fig. 6c and d, $x < 140$ m) and deposition in the bar trough ($140 < x < 200$ m), unlike the observed morphological evolution. There were no hydrodynamic measurements for $x < \sim 120$ m, and thus the

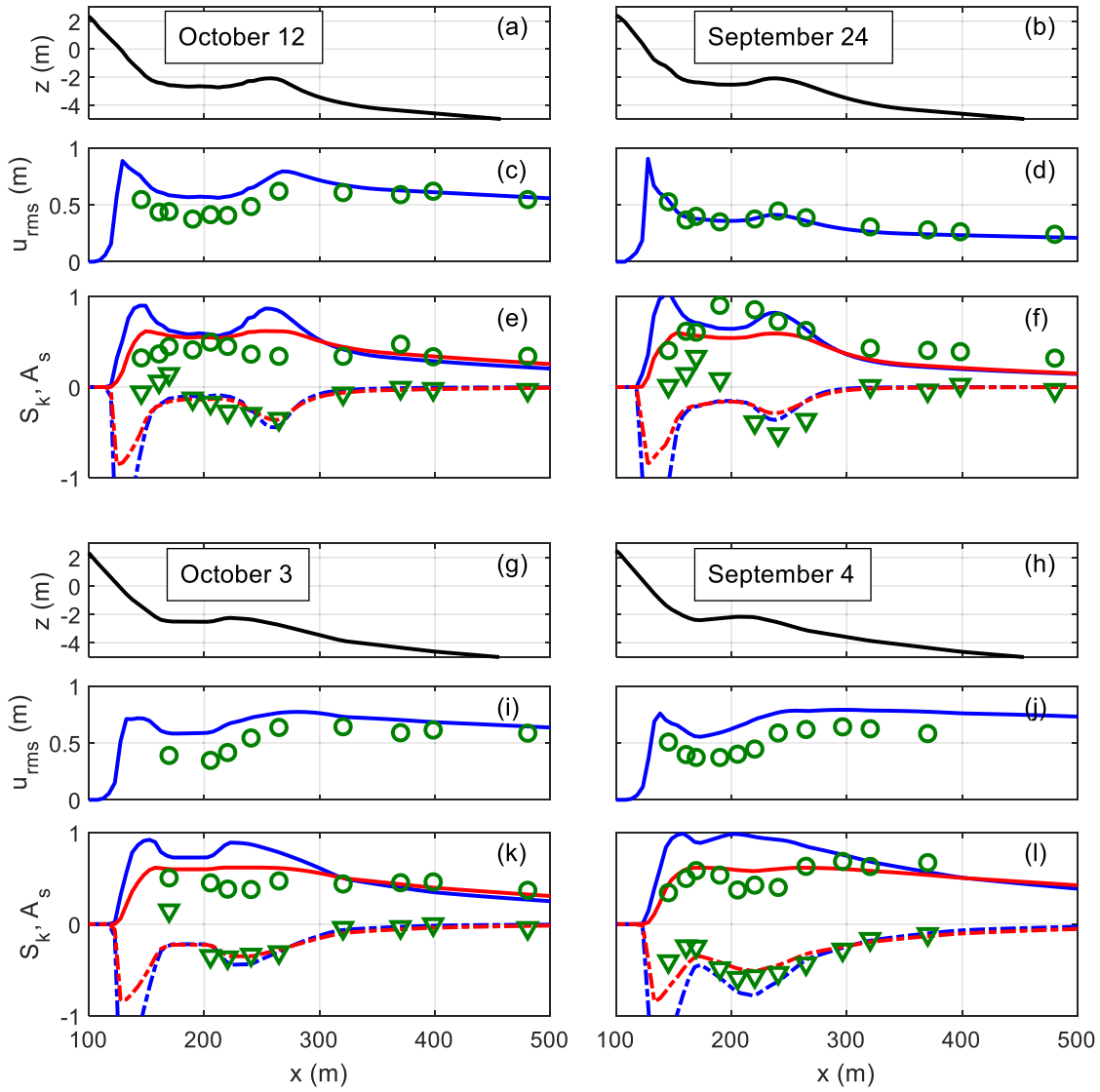

Fig. 5. (a,b,g,h) Seafloor elevation z, (c,d,i,j) root-mean-square orbital velocity u_{rms} (symbols are observations, solid-blue curves are XB-SB simulations), and (e,f,k,l) skewness (S_k) and asymmetry (A_s) versus cross-shore location for (a,c,e) Event IV (October 12, $H_{s,0} = 2.07$ m ($H_{rms,0} = 1.46$ m)), (b,d,f) Event II (September 24, $H_{s,0} = 0.70$ m ($H_{rms,0} = 0.49$ m)), (g,i,k) Event III (October 3, $H_{s,0} = 2.37$ m ($H_{rms,0} = 1.68$ m)), and (h,j,l) Event I (September 4, $H_{s,0} = 2.68$ m ($H_{rms,0} = 1.89$ m)). The third moments (e,f,k,l) are estimated from observations (green circles are skewness and green triangles are asymmetry) and XB-SB simulations (solid curves are skewness, dashed curves are asymmetry) using different parameterizations (blue curves are Van Thiel De Vries (2009) and the red curves are Ruessink et al. (2012)). (For interpretation of the references to colour in this figure legend, the reader is referred to the Web version of this article.)

Table 3
Relative mean absolute error (RMAE) between simulations and observations for H_{rms}, u_e, and u_{rms}, for 1-h runs using setup VT09_I ($\beta = 0.1$) and VT09_II (variable β, Eqn. (10)) in the sandbar region (200 m < x < 350 m).

Setup ID	H_{rms}	u_e	u_{rms}	H_{rms}	u_e	u_{rms}
	October 12, 10:00 to 11:00 EST			September 24, 12:00 to 13:00 EST		
VT09_I	0.08	0.49	0.23	0.08	0.65	0.09
VT09_II	0.07	0.24	0.22	0.08	0.65	0.09
	October 3, 13:00 to 14:00 EST			September 4, 12:00 to 13:00 EST[a]		
VT09_I	0.15	0.48	0.26	0.20	0.46	0.35
VT09_II	0.14	0.37	0.26	0.20	0.34	0.35

[a] For September 4 the bar region is defined as 150 m < x < 350 m.

cause of the over-predicted erosion is not known.

Simulations of offshore bar migration are improved by using different values of γ_{ua} depending on the third-moment parameterizations, which controls the strength of the third-moment term (Eqn. (6)). The most skillful predictions of offshore sandbar migration were obtained with $\gamma_{ua} = 0.3$ (Van Thiel De Vries (2009), Fig. 6e, Table 4, VT09_III) and $\gamma_{ua} = 0.4$ (Ruessink et al. (2012), Fig. 6h, Table 4, R12_IV). Different values of γ_{ua} needed with different wave-shape models can be justified by comparing the skewness (S_k) predictions by the two models with each other near the bar crest (Fig. 5e, October 12), where the S_k value calculated by the Van Thiel De Vries (2009) model at the bar crest is about 40% higher than that calculated by the Ruessink et al. (2012) model. Thus, a higher value of γ_{ua} would be required by Ruessink et al. (2012) to simulate accurately the cross-shore sediment transport in the bar region. Although the model skill predicting the sandbar crest was improved using $\gamma_{ua} = 0.3$–0.4 rather than the default value of $\gamma_{ua} = 0.1$, both models still predicted erosion near the shoreline that was not observed (Fig. 6e and h). Using the shoreline slope correction, the models predict no erosion near the shoreline, similar to the observations (Fig. 6i and j, Table 5, VT09_VI and R12_VI).

Simulations using the default values in XB-SB do not predict the

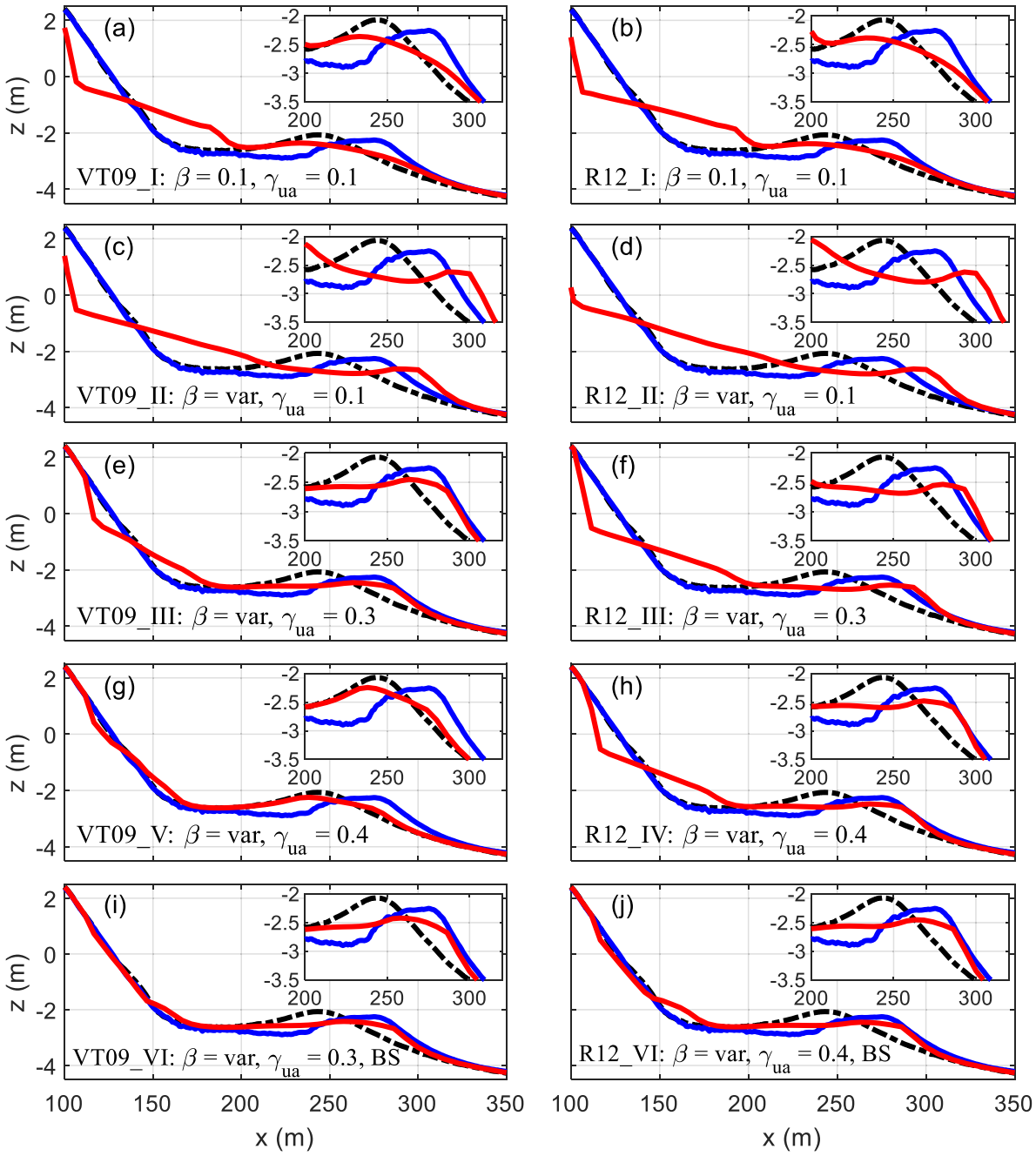

Fig. 6. Seafloor elevation observed at the start (dashed-black curves) and end (solid-blue curves) of the offshore sandbar migration Event IV (October 10 to 14) and corresponding XB-SB predictions of the seafloor elevation at the end of the event (solid-red curves) versus cross-shore location for different coefficient values used in XB-SB (listed on the bottom of each panel, see Table 1). The third-moment parameterizations used in XB-SB are (left panels, a,c,e,g,i) Van Thiel De Vries (2009) and (right panels, b,d,f,h,j) Ruessink et al. (2012). The insets show more detailed views near the sandbar. In panels (i) and (j) "BS" refers to the berm slope correction (Eqn. (7)) switched on. (For interpretation of the references to colour in this figure legend, the reader is referred to the Web version of this article.)

observed onshore sandbar migration (Fig. 7a and b, Table 4, VT09_I and R12_I). Using variable β in the roller formulation results in offshore bar migration for both wave-shape models (Fig. 7c and d, Table 4, VT09_II and R12_II), probably due to slightly larger undertow that occurred occasionally in Event II (not represented in the 1-h results presented in Fig. 3f). Similar to the offshore migration event (Fig. 6), both models predict erosion near the shoreline and deposition in the bar trough, which is not observed (Fig. 7a–d). Improved model skill is obtained by using $\gamma_{ua} = 0.35$ (Van Thiel De Vries (2009), Fig. 7e, Table 4, VT09_IV) and $\gamma_{ua} = 0.55$ (Ruessink et al. (2012), Fig. 7f, Table 4, R12_V). The higher value of γ_{ua} required by the Ruessink et al. (2012) wave-shape model can be explained by the lower S_k predicted at the bar crest compared to that predicted by Van Thiel De Vries (2009) during low-energy condition (Fig. 5 (f)). Using the shoreline slope correction, the erosion near the shoreline was avoided (Fig. 7g and h, Table 5, VT09_VII and R12_VII).

Given the proposed coefficients obtained from the offshore bar migration Event IV, XB-SB was tested by comparing simulations with the other two observed offshore bar migration events. For Event III model skill is good (Fig. 8a and b and Tables 4 and 5, VT09_VI and R12_VI). However, for Event I, during which the incident waves were somewhat higher, and high wave heights persisted for a longer period of time than

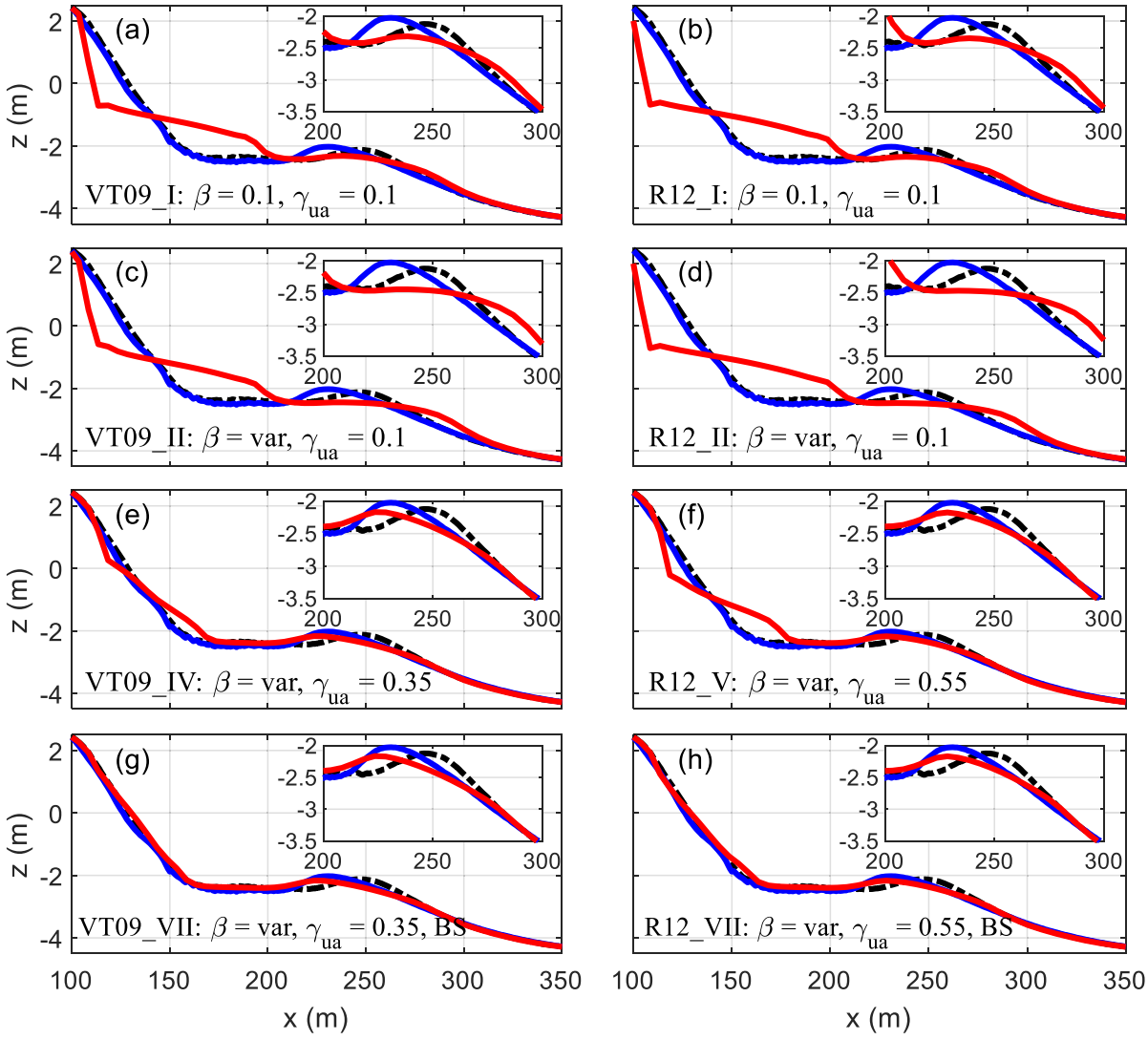

Fig. 7. Seafloor elevation observed at the start (dashed-black curves) and end (solid-blue curves) of the onshore sandbar migration event II (September 21 to 26) and corresponding XB-SB predictions of the seafloor elevation at the end of the event (solid-red curves) versus cross-shore location for different coefficient values used in XB-SB (listed on the bottom of each panel, see Table 1). The third-moment parameterizations used in XB-SB are (left panels, a,c,e,g) Van Thiel De Vries (2009) and (right panels, b,d,f,h) Ruessink et al. (2012). The insets show more detailed views near the sandbar. In panels (g) and (h) "BS" refers to the berm slope correction (Eqn. (7)) switched on. (For interpretation of the references to colour in this figure legend, the reader is referred to the Web version of this article.)

in the other events (Fig. 2e), the model has little skill and flattens out the sandbars (Fig. 8c and d, Tables 4 and 5, TV09_VI and R12_VI). This discrepancy may partially be attributed to uncertainty in the initial bathymetry, which was estimated by the spatially sparse cross-shore transect of altimeters, separated by ~35 m in the bar region.

4. Discussion

4.1. Calibrating the onshore sediment transport parameter γ_{ua}

The comparisons of the model simulations with observations of sandbar migration suggest that although a variable roller energy dissipation coefficient β (Eqn. (10)) leads to higher predictive skill than a constant β, no set of coefficients is preferred for all conditions. However, the range of proposed γ_{ua} values suggested here is narrower than the range of values in the literature (Harter and Figlus, 2017 (default γ_{ua} = 0.1); Splinter and Palmsten, 2012 (γ_{ua} = 0.15); de Vet et al., 2015 (γ_{ua} = 0.2); Schambach et al., 2018 (γ_{ua} = 0.3); Ramakrishnan et al., 2018 (γ_{ua} = 0.4)). The calibration results show that the tuned γ_{ua} is dependent on how the wave asymmetry and skewness are parameterized, and also depends on the incident wave field. Usually, lower values of γ_{ua} are needed for high-energy conditions, consistent with previous morphodynamic simulations of beach erosion and recovery (Cohn et al., 2019; Pender and Karunarathna, 2013). During high-energy conditions, when the Ruessink et al. (2012) wave-shape model simulates the cross-shore dependence of skewness and asymmetry fairly accurately (Fig. 5e,k,l), γ_{ua} = 0.4 is recommended to predict the morphodynamic evolution in the surf zone. In contrast, during low energy conditions, the Ruessink et al. (2012) wave-shape parameterization under-predicts wave skewness and asymmetry in the surf zone (Fig. 5f), and it is necessary to increase γ_{ua} to 0.55 to predict the onshore bar migration. Moreover, although Van Thiel De Vries (2009) wave-shape parameterization gives a narrower range of γ_{ua} = 0.3–0.35, it tends to over-predict wave skewness in the surf zone during energetic conditions (Fig. 5e,k,l).

The tunable coefficients in XB-SB also compensate for missing or incorrect physics in the model, similar to how the friction coefficient used in quadratic drag formulations can compensate for the neglect of advective accelerations (Apotsos et al., 2008; Hansen et al., 2015). For example, the sediment transport formulation in XB-SB does not include boundary layer streaming, which can have a significant effect on the

Table 4
Brier Skill Score (BSS) for the simulated seafloor elevation change and root mean square error (RMSE) between XB-SB simulations and observations of the final seafloor elevation in the sandbar region (200 < x < 350 m).

Setup ID	BSS	RMSE (m)	BSS	RMSE (m)
	October 10–14 (Event IV)		September 21–26 (Event II)	
VT09_I	0.44	0.29	−0.28	0.15
VT09_II	0.265	0.34	−1.94	0.23
VT09_III	0.81	0.17	–	–
VT09_IV	–	–	0.63	0.08
VT09_V	0.32	0.33	–	–
VT09_VI	0.80	0.18	–	–
VT09_VII	–	–	0.63	0.08
R12_I	0.45	0.29	−1.07	0.19
R12_II	0.08	0.38	−2.91	0.26
R12_III	0.70	0.22	–	–
R12_IV	0.79	0.18	–	–
R12_V	–	–	0.68	0.075
R12_VI	0.80	0.18	–	–
R12_VII	–	–	0.70	0.08
	September 30 – October 4 (Event III)		September 1–5 (Event I)[a]	
VT09_VI	0.86	0.07	0.32	0.28
R12_VI	0.83	0.08	0.21	0.30

[a] For Event I the bar region is defined as 150 m < x < 350 m.

Table 5
Root mean square error (RMSE) between XB-SB simulations and observations of the final seafloor elevation in the beach region onshore of the sandbar (100 < x < 200 m).

Setup ID	RMSE (m)	RMSE (m)
	October 10–14 (Event IV)	September 21–26 (Event II)
VT09_I	0.97	0.89
VT09_II	1.1	0.88
VT09_III	0.46	–
VT09_IV	–	0.29
VT09_V	0.24	–
VT09_VI	0.14	–
VT09_VII	–	0.18
R12_I	1.14	1.10
R12_II	1.15	1.10
R12_III	0.86	–
R12_IV	0.63	–
R12_V	–	0.48
R12_VI	0.27	–
R12_VII	–	0.19
	September 30 – October 4 (Event III)	September 1-5[a] (Event I)
VT09_VI	0.11	0.14
R12_VI	0.13	0.22

[a] For Event I the beach region is defined as 100 m < x < 150 m.

onshore sediment flux under progressive waves (Henderson et al., 2004; Kim et al., 2018; Kranenburg et al., 2013). XB-SB also ignores horizontal and vertical sediment size sorting (Holland and Elmore, 2008; Schwartz and Birkemeier, 2004), which can enhance or reduce the wave-driven onshore sediment transport rate by about 30% depending on the wave shape, wave intensity, and the degree of size gradation (Rafati et al., 2020). These unresolved physical processes may require a compensating role of onshore transport driven by third moments of orbital velocities (γ_{ua}). Laboratory studies can be used to investigate how the tuned γ_{ua} might compensate for unresolved physics in the model.

4.2. Multi-scale analysis of wave-induced onshore sediment transport

There are many formulations for sediment transport, including the advection-diffusion approach used in XB-SB (Eqn (AA.11), Appendix A.3) and the "practical" formula developed with extensive oscillatory-tunnel and large-flume laboratory experiments (Van der A et al., 2013, hereinafter termed "VdA") that is considered the state-of-the-art sediment transport formula synthesizing existing laboratory data for estimating the wave-period-averaged wave-driven sediment transport rate. Here, the wave-induced onshore sediment transport rates calculated by XB-SB are compared with the rates calculated by VdA. The VdA approach parameterizes the effect of wave-orbital velocity skewness and asymmetry associated with the breaking wave shape on sediment transport. However, it does not incorporate the effect of wave-breaking turbulence on the bed sediment entrainment. Large wave flume data (Van der Zanden et al., 2017) show that the wave-induced onshore sediment flux in the bar region occurs near the bed and is correlated with the wave skewness and asymmetry. Hence, unlike the inner surf and swash zones, the direct influence of wave-breaking turbulence may be of secondary importance. Nevertheless, the different roles of wave breaking in the XB-SB and VdA transport rates may introduce uncertainties when comparing them with each other.

The VdA formula calculates the wave-averaged sediment transport rate based on parameterizing the bed shear stress, incorporating the effects of wave shape, intensity, and progressive streaming. The wave-averaged sediment transport rate q_s is calculated as (Van der A et al., 2013),

$$\frac{q_s}{\sqrt{(s-1)gd_{50}{}^3}} = \frac{\sqrt{|\theta_c|}T_c\left(\Omega_{cc}+\frac{T_c}{2T_{cu}}\Omega_{tc}\right)\frac{\theta_c}{|\theta_c|}+\sqrt{|\theta_t|}T_t\left(\Omega_{tt}+\frac{T_t}{2T_{tu}}\Omega_{ct}\right)\frac{\theta_t}{|\theta_t|}}{T}, \tag{13}$$

where $s = 2.65$ is the specific gravity of sand and $d_{50} = 0.2$ mm is the median diameter of the sand. Subscripts "c" and "t" refer to wave crest (onshore flow) and trough (offshore flow) intervals. Thus, T_c and T_t represent the crest and trough periods, respectively, and T_{cu} and T_{tu} are the "acceleration" time intervals during the crest and trough periods, respectively (Fig. 9). θ_c and θ_t are the non-dimensional bed shear stresses for the wave crest and trough periods. The non-dimensional Ω accounts for phase lag between suspension and transport, with Ω_{ct} (Ω_{tc}) the sediment load entrained during the crest (trough) interval and transported during the trough (crest) interval, and thus this term reduces (increases) onshore transport. The bed shear stress, incorporating the effect of progressive wave streaming, is given by,

$$\theta_i = |\theta_i|\frac{u_{i,r}}{|u_{i,r}|}+\frac{\tau_{wRe}}{(s-1)gd_{50}}, \tag{14}$$

where i refers to wave crest (c) or trough (t), and $u_{i,r}$ is the representative wave-orbital velocity amplitude during the crest or trough interval. The bed shear stress, τ_{wRe} incorporates the contribution from progressive wave streaming which is parameterized as,

$$\tau_{wRe} = \rho\frac{f_w}{2c_w}\alpha_w\widehat{u}^3, \tag{15}$$

where f_w is the wave friction factor, c_w is the wave celerity, $\alpha_w = 4/3\pi$, and $\widehat{u}$ is the representative velocity amplitude for the entire flow period (Van der A et al., 2013).

A representative time series of near-bed wave-orbital velocity is required to calculate the wave-driven sediment transport rate q_{wave}. Here, a representative near-bed wave-orbital velocity time series was determined using an analytical formula (Abreu et al., 2010) for three locations spanning the sandbar crest for each of the three offshore bar migration events (Table 6). The representative time series reproduces the root-mean-square wave-orbital velocity, skewness, and asymmetry simulated by XB-SB for a given 1-h observational period. The near-bed wave-orbital velocities during high-energy conditions associated with the observed offshore bar migration (Table 6) are similar in magnitude to those in laboratory experiments of wave-induced sediment transport

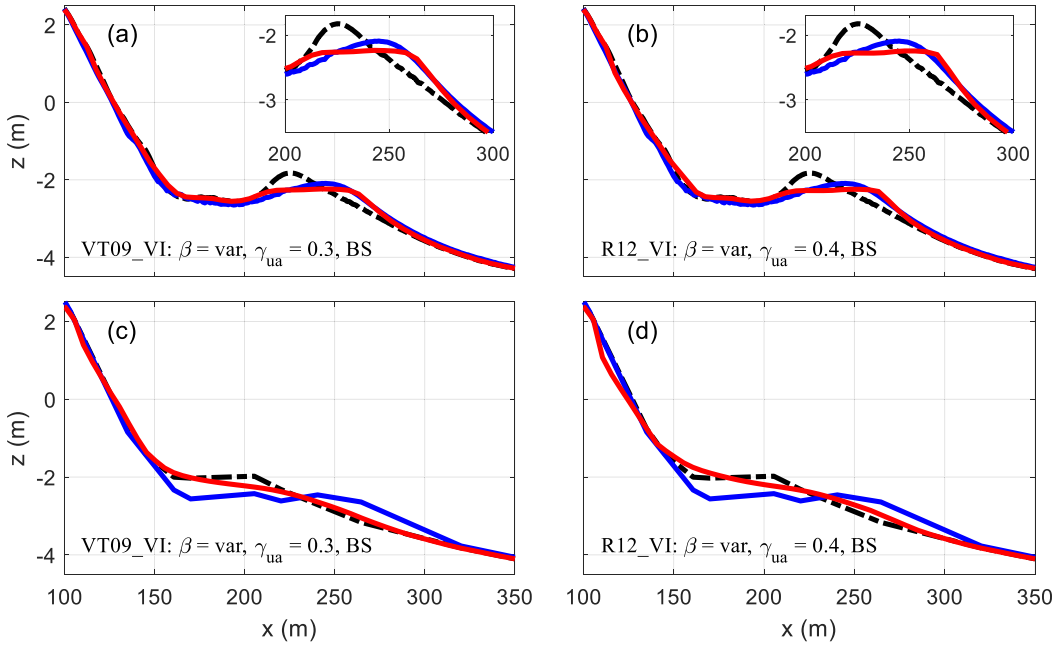

Fig. 8. Seafloor elevation observed at the start (dashed-black curves) and end (solid-blue curves) of (a,b) the offshore migration Event III (September 30 to October 4) and (c,d) the offshore migration Event I (September 1 to 5) and the corresponding XB-SB predictions of the seafloor elevation at the end of the events (solid-red curves) versus cross-shore location for different coefficient values used in XB-SB (listed on the bottom of each panel, see Table 1). The insets show more detailed views near the sandbar. "BS" refers to the berm slope correction (Eqn. (7)) switched on. (For interpretation of the references to colour in this figure legend, the reader is referred to the Web version of this article.)

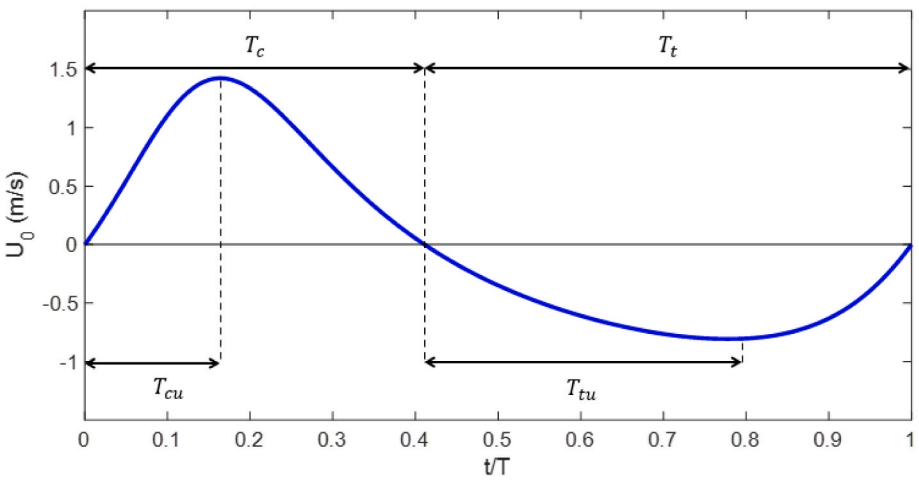

Fig. 9. Wave-orbital velocity versus time normalized by the wave period for a representative time series (Abreu et al., 2010) with the same root-mean-square velocity, skewness, and asymmetry as simulated by XB-SB using the Ruessink et al. (2012) third-moment parameterization for a 1-hr model run for October 12 (Table 6) at the bar crest (x = 257.9 m). The wave crest (T_c), wave trough (T_t), and the acceleration intervals (T_{cu} and T_{tu}) are used in the VdA (Van der A et al., 2013) sand transport formula.

in the sheet flow regime (Dibajnia and Watanabe, 1992; O'Donoghue and Wright, 2004; Van der A et al., 2010).

To estimate the corresponding wave-induced sediment transport rate from XB-SB, model runs with γ_{ua} = 0.1, 0.3, and 0.4 (driven by waves and mean currents) were compared with a run with γ_{ua} = 0.0 (driven by mean currents only) (Fig. 10). During the offshore migration events, the total transport (waves and currents) is offshore directed and decreases as the wave-driven transport coefficient γ_{ua} is increased (Fig. 10a), consistent with the increasing amounts of onshore sediment transport driven by waves only as γ_{ua} is increased (Fig. 10b).

For a low value of γ_{ua} = 0.1, wave-induced onshore transport rates predicted by XB-SB are less than those predicted by the VdA formula (Fig. 11a). Wave-induced transport in XB-SB is proportional to γ_{ua}, and thus increasing γ_{ua} by a factor of 3 or 4 increases transport by the same amount, leading to a better agreement (within a factor two) with VdA (Fgure11b,c). The best correspondence between XB-SB and VdA transport rates is for γ_{ua} = 0.3–0.4, for which RMSE errors are on the order of 45–50% (Fig. 11b and c). Interestingly, consistent with the tuning of γ_{ua} with the two wave-shape parameterizations performed in Section 3.4, it can be seen that using γ_{ua} = 0.3 with the wave-shape model of Van Thiel De Vries (2009) (Fig. 11b, blue symbols, best fit line slope of 1.7) and using γ_{ua} = 0.4 with the wave-shape model of Ruessink et al. (2012) (Fig. 11c, red symbols, best fit line slope of 1.8) both show good agreement with the transport rates predicted by VdA. These proposed values are nearly the same as those obtained by matching XB-SB simulations with observations of sandbar migration (γ_{ua} = 0.3–0.4). Specifying γ_{ua} = 0.3–0.4 in the XB-SB onshore sediment transport parameterization also agrees with the VdA formula in the sheet flow

Table 6
Locations (x) spanning the sandbar crest, and corresponding root-mean-square velocities (U_{rms}), and skewness (S_k) and asymmetry (As) for the two parameterizations of wave shapes for the three offshore sandbar migration events. The statistics are the same for XB-SB and for the representative time series.

	x (m)	U_{rms} (m/s)	wave-shape: Van Thiel De Vries (2009)		wave-shape: Ruessink et al. (2012)	
			S_k	A_s	S_k	A_s
September 4,	198.2	0.62	0.97	−0.65	0.60	−0.45
$H_{s,0}$ = 2.68 m	213.2	0.67	0.97	−0.75	0.59	−0.49
	228.2	0.73	0.94	−0.71	0.59	−0.49
October 3,	207.6	0.59	0.75	−0.25	0.60	−0.24
$H_{s,0}$ = 2.37 m	222.6	0.67	0.90	−0.45	0.62	−0.36
	252.7	0.74	0.83	−0.38	0.62	−0.32
October 12,	237.9	0.64	0.76	−0.26	0.61	−0.25
$H_{s,0}$ = 2.07 m	257.9	0.75	0.87	−0.46	0.62	−0.36
	272.9	0.79	0.77	−0.32	0.61	−0.29

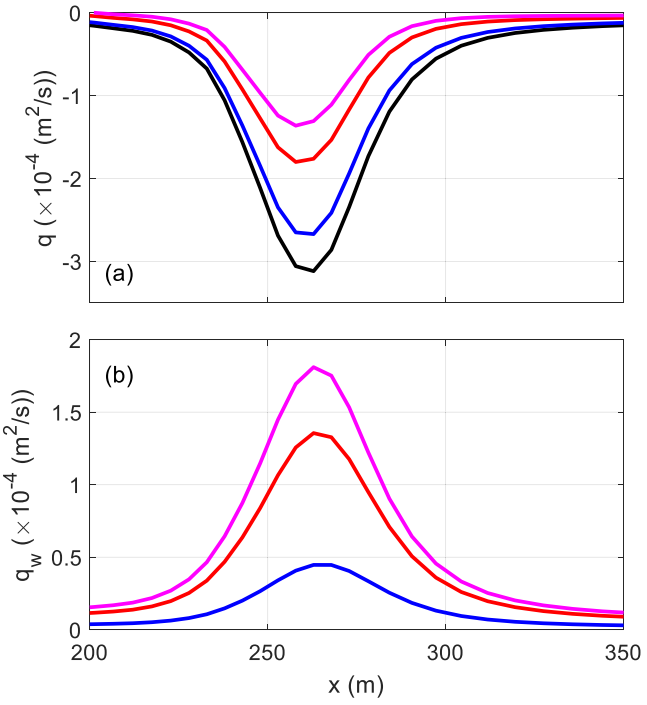

Fig. 10. XB-SB simulated (a) total (wave + current driven) transport rate (positive onshore) and (b) wave-only driven transport rate versus cross-shore location for a 1-hr model run for October 12 (Table 6) in the sandbar region (200 m < x < 350 m). All simulations use the variable β (roller dissipation) formulation (Eqn. (10)) and the third-moment parameterization of Ruessink et al. (2012), with the wave-driven onshore transport parameter varying from γ_{ua} = 0 (black, no waves), to 0.1 (blue), 0.3 (red), and 0.4 (magenta). (For interpretation of the references to colour in this figure legend, the reader is referred to the Web version of this article.)

regime, which is calibrated extensively with laboratory data, providing additional physical evidence for using γ_{ua} = 0.3–0.4.

The VdA formulation includes both asymmetrical-wave- and bottom-boundary-layer-streaming-induced onshore transport, allowing investigation of the relative importance of these mechanisms during the energetic offshore sandbar migration events. Bottom-boundary-layer streaming contributes approximately 35–50% to the wave-driven onshore transport predicted by the VdA formulation (compare Fig. 12a with Fig. 12b). The significance of bottom-boundary-layer streaming is consistent with the two-phase, free-surface-resolving model simulations of observations made in large wave flumes and oscillatory tunnels (Kim et al., 2019), suggesting that, depending on wave skewness and asymmetry, bottom-boundary-layer streaming contributes approximately 30–70% to the wave-driven onshore transport. XB-SB does not include an explicit parameterization of bottom-boundary-layer streaming nor of the corresponding onshore sediment transport. However, some of the effects of streaming may be accounted for by increasing the strength of asymmetrical wave-driven onshore transport (γ_{ua}). The VdA formulation does not include the sediment entrainment by wave-breaking turbulence. Therefore, it is possible that a portion of the bottom-boundary-layer streaming effect in VdA compensates for sediment entrainment by wave-breaking turbulence.

5. Conclusions

Numerical simulations with XBeach-Surfbeat (XB-SB) were compared with observations of waves, currents, and bathymetric evolution during three offshore sandbar migration events and one onshore migration event in the surf zone on an Atlantic Ocean beach for a range of incident wave conditions. The simulated offshore-directed mean current (undertow), the main driver of offshore sediment transport in the wave breaking region and inner surf zone is sensitive to the roller energy model. Here, simulations using a new formulation for the roller-energy dissipation term that varies in the cross-shore as a function of local wave characteristics were more skillful predicting the observed undertow when energetic incident waves broke on the sandbar than were simulations using the default constant coefficient.

The modeled onshore sediment transport is sensitive to the parameterization of non-sinusoidal wave shapes (i.e., nonzero third moments, skewness and asymmetry), and to the strength of the corresponding wave-orbital-velocity-driven transport (γ_{ua} parameter). The best coefficient for one third-moment parameterization may be different than the best coefficient for a different parameterization. The proposed combination of third-moment parameterization and adjustable coefficient also depends on the incident wave conditions. Given a particular third-moment parameterization, the best coefficient found during an offshore sandbar migration event may not be the best coefficient during an onshore migration event. Model results suggest that the wave-shape model of Ruessink et al. (2012) has good skill simulating the cross-shore evolution of wave skewness and asymmetry during high energy events, and combined with the sediment transport parameter γ_{ua} = 0.4 simulates offshore sandbar migration during storms fairly accurately. In contrast, the Van Thiel De Vries (2009) wave-shape model over-predicts wave skewness during energetic events, and thus the proposed onshore sediment transport parameter is lower (γ_{ua} = 0.30). During less energetic waves, the Ruessink et al. (2012) wave-shape model under-predicts the wave skewness and asymmetry in the bar region and inner surf zone, and thus simulating the onshore bar migration requires a higher value of γ_{ua} = 0.55. However, the Van Thiel De Vries (2009) approach predicts higher velocity skewness near the bar crest, and the calibrated γ_{ua} = 0.35 works well to simulate the observed onshore bar migration. One reason the proposed coefficients are event-specific for simulating sandbar migration may be that the accuracy of the wave-shape models depends on incident wave conditions and the bathymetry.

The proposed values for the coefficient determining the strength of onshore sediment transport driven by non-sinusoidal wave-orbital velocities (γ_{ua}) are similar to the values that align XB-SB transport rates with those predicted by the Van der A et al. (2013) formula that includes transport driven both by asymmetrical wave shapes and by bottom-boundary-layer streaming. Increasing the coefficient for wave-driven (onshore) transport (γ_{ua}) in XB-SB from its default value may compensate for the neglect of boundary-layer streaming (and possibly other processes such as grain size sorting).

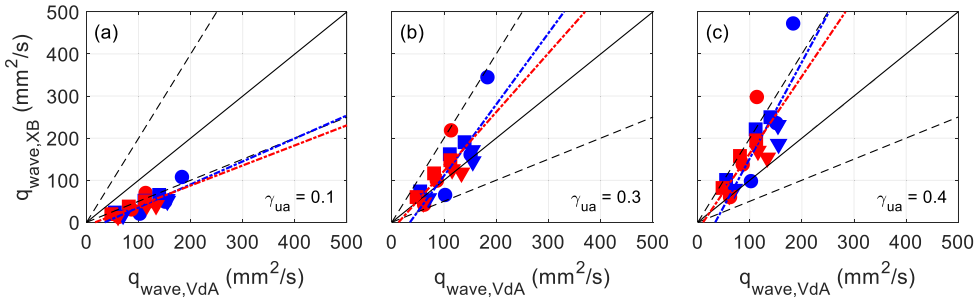

Fig. 11. Wave-driven onshore sediment transport rates estimated by XB-SB versus the transport rate estimated by the VdA formula (Van der A et al., 2013) for locations spanning the sandbar crest (Table 6) for γ_{ua} = (a) 0.1, (b) 0.3, and (c) 0.4. The three offshore migration events are Event I (September 4, $H_{s,0}$ = 2.68 m, circles), Event III (October 3, $H_{s,0}$ = 2.37 m, squares), and Event IV (October 12, $H_{s,0}$ = 2.07 m, triangles). The third-moment parameterizations used in XB-SB are shown by the blue (Van Thiel De Vries, 2009) and red (Ruessink et al., 2012) symbols. Least squares best fits are shown with the dash-dot blue (Van Thiel De Vries, 2009) and red (Ruessink et al., 2012) lines. One-to-one correspondence between the two transport rates is shown by the solid-black lines, and the dashed-black lines have slopes one-half and twice the slope of the one-to-one lines. (For interpretation of the references to colour in this figure legend, the reader is referred to the Web version of this article.)

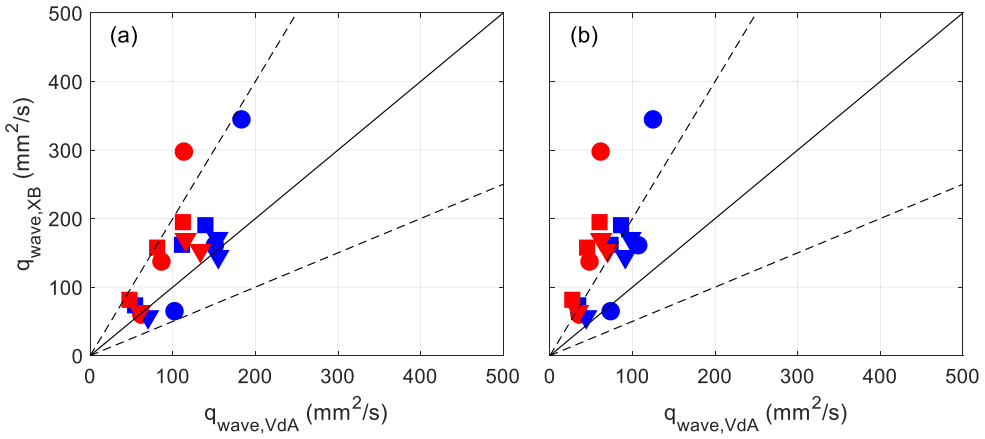

Fig. 12. Wave-driven onshore sediment transport rates estimated by XB-SB versus transport rates estimated by the VdA formula (Van der A et al., 2013) (a) including and (b) neglecting bottom-boundary-layer streaming for locations spanning the sandbar crest (Table 6). The three offshore migration events are Event I (September 4, $H_{s,0}$ = 2.68 m, circles), Event III (October 3, $H_{s,0}$ = 2.37 m, squares), and Event IV (October 12, $H_{s,0}$ = 2.07 m, triangles). The third-moment parameterizations and γ_{ua} used in XB-SB are shown by the blue (γ_{ua} = 0.3, Van Thiel De Vries, 2009) and red (γ_{ua} = 0.4, Ruessink et al., 2012) symbols. One-to-one correspondence between the two transport rates is shown by the solid-black lines, and the dashed-black lines have slopes one-half and twice the slope of the one-to-one lines. (For interpretation of the references to colour in this figure legend, the reader is referred to the Web version of this article.)

CRediT authorship contribution statement

Yashar Rafati: Conceptualization, Methodology, Software, Investigation, Writing – original draft, Visualization. **Tian-Jian Hsu:** Conceptualization, Methodology, Writing – original draft, Supervision, Project administration, Funding acquisition. **Steve Elgar:** Methodology, Resources, Writing – review & editing. **Britt Raubenheimer:** Methodology, Resources, Writing – review & editing. **Ellen Quataert:** Methodology, Software. **Ap van Dongeren:** Methodology, Software, Writing – review & editing.

Declaration of competing interest

The authors declare that they have no known competing financial interests or personal relationships that could have appeared to influence the work reported in this paper.

Acknowledgments

We thank R. Guza and T. Herbers for their leadership roles during the fieldwork, and the CCS (SIO), PVLAB (WHOI), and FRF (USACE) field teams for deploying, maintaining, and recovering sensors for several months in harsh conditions. Funding was provided by the Office of Naval Research, the National Science Foundation, a Vannevar Bush Faculty Fellowship (OUSD(R&E)), Sea Grant, the United States Coastal Research Program, and WHOI ISP. XBeach is a public domain open-source model, which can be accessed at https://oss.deltares.nl/web/xbeach/download.

Appendix. Model details

A.1. Shallow water equations

XB-SB solves the nonlinear shallow water momentum and continuity equations, given by,

$$\frac{\partial u^L}{\partial t}+u^L\frac{\partial u^L}{\partial x}+v^L\frac{\partial u^L}{\partial y}-\nu_h\left(\frac{\partial^2 u^L}{\partial x^2}+\frac{\partial^2 u^L}{\partial y^2}\right)=-\frac{\tau_{bx}}{\rho h}-g\frac{\partial \eta}{\partial x}+\frac{F_x}{\rho h}, \tag{AA.1}$$

$$\frac{\partial v^L}{\partial t}+u^L\frac{\partial v^L}{\partial x}+v^L\frac{\partial v^L}{\partial y}-\nu_h\left(\frac{\partial^2 v^L}{\partial x^2}+\frac{\partial^2 v^L}{\partial y^2}\right)=-\frac{\tau_{by}}{\rho h}-g\frac{\partial \eta}{\partial y}+\frac{F_y}{\rho h}, \tag{AA.2}$$

$$\frac{\partial \eta}{\partial t}+\frac{\partial hu^L}{\partial x}+\frac{\partial hv^L}{\partial y}=0, \tag{AA.3}$$

where t is time, u^L and v^L are the depth-averaged Lagrangian velocities, x and y are the cross- and alongshore coordinates, respectively, η is the water level, g is the gravitational acceleration, ρ is water density, τ_{bx} and τ_{by} are the bed shear stresses, h is water depth, and ν_h is the horizontal viscosity. The wave-induced stresses F_x and F_y are calculated based on radiation stress contributions from short wave action and wave roller energy as,

$$F_x=-\left(\frac{\partial S_{xx,w}+\partial S_{xx,r}}{\partial x}+\frac{\partial S_{xy,w}+\partial S_{xy,r}}{\partial y}\right), \tag{AA.4}$$

$$F_y=-\left(\frac{\partial S_{xy,w}+\partial S_{xy,r}}{\partial x}+\frac{\partial S_{yy,w}+\partial S_{yy,r}}{\partial y}\right), \tag{AA.5}$$

where $S_{xx,w}$, $S_{yy,w}$, and $S_{xy,w}$ are the radiation stress components from the wave action and $S_{xx,r}$, $S_{yy,r}$, and $S_{xy,r}$ are the radiation stress components from roller energy.

A.2. Wave action equation

The variation of the short-wave envelope is tracked by solving the wave action (A) equation,

$$\frac{\partial A}{\partial t}+\frac{\partial c_x A}{\partial x}+\frac{\partial c_y A}{\partial y}+\frac{\partial c_\phi A}{\partial \phi}=\frac{D_w+D_f}{\sigma}, \tag{AA.6}$$

where ϕ is the angle of incidence with respect to the x-axis, D_w and D_f are the dissipation by wave breaking and bottom friction, respectively, c_x, c_y, and c_ϕ are the wave celerities in the x, y, and ϕ direction, respectively. The wave action is defined as,

$$A(x,y,t,\theta)=\frac{S_w(x,y,t,\phi)}{\sigma(x,y,t)}, \tag{AA.7}$$

where S_w is the wave energy density in each directional bin and σ is the intrinsic wave frequency. The radiation stress induced by the short-wave action is obtained by integrating the wave energy density over the directional bins,

$$S_{xx,w}(x,y,t)=\int\left(\frac{c_g}{c}\left(1+cos^2\phi\right)-\frac{1}{2}\right)S_w d\phi, \tag{AA.8}$$

$$S_{xy,w}(x,y,t)=S_{yx,w}=\int sin\phi cos\phi\left(\frac{c_g}{c}S_w\right)d\phi, \tag{AA.9}$$

$$S_{yy,w}(x,y,t)=\int\left(\frac{c_g}{c}\left(1+sin^2\phi\right)-\frac{1}{2}\right)S_w d\phi, \tag{AA.10}$$

where c_g and c are the group velocity and wave celerity, respectively, obtained from linear wave theory.

A.3. Sediment transport formulation

Sediment transport is calculated by solving an advection-diffusion equation to obtain the depth-averaged sediment concentration C, given by (Galappatti and Vreugdenhil, 1985)

$$\frac{\partial hC}{\partial t}+\frac{\partial hC(u^E-u_a sin\phi)}{\partial x}+\frac{\partial hC(v^E-u_a cos\phi)}{\partial y}+\frac{\partial}{\partial x}\left[D_h h\frac{\partial C}{\partial x}\right]+\frac{\partial}{\partial y}\left[D_h h\frac{\partial C}{\partial y}\right]=\frac{hC_{eq}-hC}{T_s}, \tag{AA.11}$$

where u^E and v^E are the Eulerian velocities in the x and y directions, respectively, u_a is an advective velocity to incorporate the effect of wave nonlinearity, D_h is the sediment diffusivity coefficient, and T_s is the adaptation time characterizing the sediment entrainment. The source term C_{eq} is the depth-averaged equilibrium concentration parameterized as (Van Thiel De Vries, 2009),

$$C_{eq}=max\left[min\left(C_{eq,b},0.5C_{max}\right)+min\left(C_{eq,s},0.5C_{max}\right),0\right], \tag{AA.12}$$

where C_{max} is the upper limit of the depth-averaged sediment concentration set to $C_{max}=0.1$. The components of the equilibrium concentration corresponding to the bed-load, $C_{eq,b}$ and suspended load, $C_{eq,s}$ are given by

$$C_{eq,b}=\frac{A_{sb}}{h}\left[\sqrt{v_{mg}^2+0.64u_{rms,2}^2}-U_{cr}\right]^{1.5}, \tag{AA.13}$$

$$C_{eq,s} = \frac{A_{ss}}{h}\left[\sqrt{v_{mg}^2 + 0.64u_{rms,2}^2} - U_{cr}\right]^{2.4}, \tag{AA.14}$$

where $v_{mg} = \sqrt{(u^E)^2 + (v^E)^2}$ is the magnitude of the Eulerian velocity including both the cross- and alongshore components, the coefficients A_{sb}, A_{ss}, and the critical velocity U_{cr} are from the literature (Van Rijn, 2007a, 2007b), and $u_{rms,2}$ is the corrected wave-orbital velocity used to obtain the equlibrium concentration using the wave-orbital velocity calculated from the short-wave action equation (u_{rms}),

$$u_{rms} = \frac{\pi H_{rms}}{T_{rep}\sqrt{2}sinh(k(h + \delta H_{rms}))}, \tag{AA.15}$$

where H_{rms} is the root-mean-square wave height, T_{rep} is a representative wave period, and δ is a coefficient with the default value of zero. The correction allows incorporating the effect of short-wave-breaking turbulence on stirring up bed sediment (Reniers et al., 2004) as follows,

$$u_{rms,2} = \sqrt{u_{rms}^2 + 1.45k_b}, \tag{AA.16}$$

where k_b is the wave breaking turbulent kinetic energy approaching the seabed, calculated using a decay function based on a mixing length applied to the wave breaking induced turbulence at the water surface. Wave-averaged (A.17) and bore-averaged (A.18) formulations describing the near-bed turbulence, respectively are given by:

$$k_b = \frac{k_s}{exp(h/L_{mix}) - 1}, \tag{AA.17}$$

$$k_b = \frac{k_s . T_{rep}/T_{bore}}{exp(h/L_{mix}) - 1}, \tag{AA.18}$$

where T_{bore} is the bore interval, k_s is the wave breaking induced turbulence at the water surface, and L_{mix} is the mixing length, given by,

$$k_s = (D_r/\rho)^{2/3}, \tag{AA.19}$$

$$L_{mix} = \sqrt{\frac{2E_r T_{rep}}{\rho c}}, \tag{AA.20}$$

where D_r is the roller energy dissipation and E_r is the roller energy.

A.4. Wave skewness and asymmetry parameterizations

XB-SB includes two parameterizations to calculate the wave skewness and asymmetry. In one wave-shape parameterization (Van Thiel De Vries, 2009), the wave skewness and asymmetry are calculated using a lookup table based on the non-dimensional wave period ($T_{rep}\sqrt{g/h}$) and wave height (H_{rms}/h). This lookup table has been prepared using stream function theory (Rienecker and Fenton, 1981). The intra-wave time series of near-bed wave orbital velocity ($u_{bed}(t)$) was then described as (Van Thiel De Vries, 2009),

$$u_{bed}(t) = \sum_{i=1}^{8} wA_i cos(i\omega t) + (1 - w)A_i sin(i\omega t), \tag{AA.21}$$

where i refers to the ith harmonic, ω is the wave angular frequency, A_i is the amplitude of ith harmonic, and w is a weighting function representing the wave shape with $w = 1$ and $w = 0$ corresponding to purely skewed (sharp, narrow peaks and broad, flat troughs) and purely asymmetric (sawtooth shaped) waves, respectively. The A_i amplitudes also are calculated using the lookup table based on $T_{rep}\sqrt{g/h}$ and wave height $H_{rms}/\ h$. There is a unique relationship between the weighting function w and the phase $\varphi = tan^{-1}(A_s/S_k)$ (Van Thiel De Vries, 2009) given by,

$$w = 0.2719ln\left(\left|\frac{\varphi - 1.8642}{0.2933 - \varphi}\right|\right) + 0.5, \tag{AA.22}$$

By having all the coefficients required for the representative time series of near-bed wave velocity (A. 21), the bore interval T_{bore} used in the bore-averaged formulation of the near-bed wave-induced turbulence (A.18) is also calculated using the lookup table.

In the other wave-shape parameterization (Ruessink et al., 2012), the wave skewness and asymmetry are calculated as a function of the Ursell number (Eqn. (8)) as,

$$S_k = Bcos\varphi, A_s = Bsin\varphi, \tag{AA.23}$$

where B is a measure of the total nonlinearity ($B = \sqrt{{S_k}^2 + {A_s}^2}$). The parameters B and φ are calculated as (Ruessink et al., 2012),

$$B = p_1 + \frac{p_2 - p_1}{1 + exp\frac{p_3 - logUr}{p_4}}, \tag{AA.24}$$

$$\varphi = -90^\circ + 90^\circ tanh(p_5/Ur^{p_6}), \tag{AA.25}$$

where the coefficients are $p_1 = 0$, $p_2 = 0.857$, $p_3 = -0.471$, $p_4 = 0.297$, $p_5 = 0.815$, $p_6 = 0.672$.

Table AA.1
List of model coefficients

category	parameter	description	used value/type
wave breaking	break	wave breaker formulation	roelvink2
	gamma	wave breaker index	0.55
	alpha	wave dissipation coefficient	1.0
	delta	fraction of wave height to add to water depth	0.0
	n	power in the dissipation model	10.0
bed friction	bedfriction	bed friction formulation	chezy
	bedfriccoef	bed friction coefficient	55.0
sediment transport	form	formulation of equilibrium sediment concentration	vanthiel_vanrijn
	Tsmin	minimum adaptation time scale	0.5
	cmax	upper limit of equilibrium sediment concentration	0.1
morphology	morfac	morphological acceleration factor	10.0
	wetslp	critical avalanching slope under water	0.3
	dryslp	critical avalanching slope above water	1.0

References

Abreu, T., Silva, P.A., Sancho, F., Temperville, A., 2010. Analytical approximate wave form for asymmetric waves. Coast. Eng. 57, 656–667. https://doi.org/10.1016/j.coastaleng.2010.02.005.

Apotsos, A., Raubenheimer, B., Elgar, S., Guza, R.T., 2008. Wave-driven setup and alongshore flows observed onshore of a submarine canyon. J. Geophys. Res. Ocean. 113, 1–9. https://doi.org/10.1029/2007JC004514.

Bailard, J.A., 1981. An energetics total load sediment transport model for a plane sloping beach. J. Geophys. Res. 86, 10938–10954.

Berard, N.A., Mulligan, R.P., da Silva, A.M.F., Dibajnia, M., 2017. Evaluation of XBeach performance for the erosion of a laboratory sand dune. Coast. Eng. 125, 70–80. https://doi.org/10.1016/j.coastaleng.2017.04.002.

Cohn, N., Hoonhout, B.M., Goldstein, E.B., de Vries, S., Moore, L.J., Vinent, O.D., Ruggiero, P., 2019. Exploring marine and aeolian controls on coastal foredune growth using a coupled numerical model. J. Mar. Sci. Eng. 7, 1–25. https://doi.org/10.3390/jmse7010013.

de Vet, P.L.M., McCall, R.T., Den Bieman, J.P., Stive, M.J.F., Van Ormondt, M., 2015. Modelling dune erosion, overwash and breaching at fire island (NY) during hurricane sandy. In: Coastal Sediments 2015. https://doi.org/10.1142/9789814689977_0006.

Dibajnia, M., Moriya, T., Watanabe, A., 2001. A representative wave model for estimation of nearshore local transport rate. Coast Eng. J. 43 (1), 1–38. https://doi.org/10.1142/S0578563401000256.

Dibajnia, M., Watanabe, A., 1992. Sheet flow under nonlinear waves and currents. In: 23rd International Conference on Coastal Engineering, pp. 2015–2028. Venice, Italy.

Doering, J.C., Bowen, A.J., 1995. Parametrization of orbital velocity asymmetries of shoaling and breaking waves using bispectral analysis. Coast. Eng. 26, 15–33. https://doi.org/10.1016/0378-3839(95)00007-X.

Drake, G., Calantoni, J., 2001. Discrete particle model for sheet flow sediment transport in the nearshore. J. Geophys. Res. 106 https://doi.org/10.1029/2000JC000611, 19859–19868.

Dubarbier, B., Castelle, B., Marieu, V., Ruessink, G., 2015. Process-based modeling of cross-shore sandbar behavior. Coast. Eng. 95, 35–50. https://doi.org/10.1016/j.coastaleng.2014.09.004.

Elgar, S., Gallagher, E.L., Guza, R.T., 2001. Nearshore sandbar migration. J. Geophys. Res. Ocean. 106, 11623–11627. https://doi.org/10.1029/2000JC000389.

Elgar, S., Guza, R.T., 1985. Observation of bispectra of shoaling surface gravity waves. J. Fluid Mech. 161, 425–448. https://doi.org/10.1017/S0022112085003007.

Elgar, S., Guza, R.T., Freilich, M.H., 1988. Eulerian measurements of horizontal accelerations in shoaling gravity waves. J. Geophys. Res. 93, 9261–9269. https://doi.org/10.1029/JC093iC08p09261.

Elsayed, S.M., Oumeraci, H., 2017. Effect of beach slope and grain-stabilization on coastal sediment transport: an attempt to overcome the erosion overestimation by XBeach. Coast. Eng. 121, 179–196. https://doi.org/10.1016/j.coastaleng.2016.12.009.

Fernández-Mora, A., Calvete, D., Falqués, A., De Swart, H.E., 2015. Onshore sandbar migration in the surf zone: new insights into the wave-induced sediment transport mechanisms. Geophys. Res. Lett. 42, 2869–2877. https://doi.org/10.1002/2014GL063004.

Galappatti, G., Vreugdenhil, C.B., 1985. A depth-integrated model for suspended sediment transport. J. Hydraul. Res. 23, 359–377. https://doi.org/10.1080/00221688509499345.

Gallagher, E.L., Elgar, S., Guza, R.T., 1998. Observations of sand bar evolution on a natural beach. J. Geophys. Res. 103, 3203–3215. https://doi.org/10.1029/97JC02765.

Garcez Faria, A.F., Thornton, E.B., Lippmann, T.C., Stanton, T.P., 2000. Undertow over a barred beach. J. Geophys. Res. 105, 16999–17010. https://doi.org/10.1029/2000JC900084.

Hansen, J.E., Raubenheimer, B., List, J.H., Elgar, S., 2015. Modeled alongshore circulation and force balances onshore of a submarine canyon. J. Geophys. Res. Ocean. 120 (3) https://doi.org/10.1002/2014JC010555, 1887–1903.

Harter, C., Figlus, J., 2017. Numerical modeling of the morphodynamic response of a low-lying barrier island beach and foredune system inundated during Hurricane Ike using XBeach and CSHORE. Coast. Eng. 120, 64–74. https://doi.org/10.1016/j.coastaleng.2016.11.005.

Henderson, S.M., Allen, J.S., Newberger, P.A., 2004. Nearshore sandbar migration predicted by an eddy-diffusive boundary layer model. J. Geophys. Res. C Oceans 109, 1–15. https://doi.org/10.1029/2003JC002137.

Hoefel, F., Elgar, S., 2003. Wave-induced sediment transport and sandbar migration. Science 299, 1885–1887. https://doi.org/10.1126/science.1081448.

Holland, K.T., Elmore, P.A., 2008. A review of heterogeneous sediments in coastal environments. Earth Sci. Rev. 89, 116–134. https://doi.org/10.1016/j.earscirev.2008.03.003.

Hoonhout, B., 2018. XBeach Documentation: Release XBeach v1.23.5527 XBeachX FINAL.

Hsu, T.J., Elgar, S., Guza, R.T., 2006. Wave-induced sediment transport and onshore sandbar migration. Coast. Eng. 53, 817–824. https://doi.org/10.1016/j.coastaleng.2006.04.003.

Hsu, T.J., Hanes, D.M., 2004. Effects of wave shape on sheet flow sediment transport. J. Geophys. Res. Ocean. 109, 1–15. https://doi.org/10.1029/2003JC002075.

Kalligeris, N., Smit, P.B., Ludka, B.C., Guza, R.T., Gallien, T.W., 2020. Calibration and assessment of process-based numerical models for beach profile evolution in southern California. Coast. Eng. 158, 103650. https://doi.org/10.1016/j.coastaleng.2020.103650.

Kim, Y., Cheng, Z., Hsu, T.-J., Chauchat, J., 2018. A numerical study of sheet flow under monochromatic nonbreaking waves using a free surface resolving Eulerian two-phase flow model. J. Geophys. Res. Ocean. 123 https://doi.org/10.1029/2018JC013930.

Kim, Y., Mieras, R.S., Cheng, Z., Anderson, D., Hsu, T.J., Puleo, J.A., Cox, D., 2019. A numerical study of sheet flow driven by velocity and acceleration skewed near-breaking waves on a sandbar using SedWaveFoam. Coast. Eng. 152 https://doi.org/10.1016/j.coastaleng.2019.103526.

Kranenburg, W.M., Ribberink, J.S., Schretlen, J.J.L.M., Uittenbogaard, R.E., 2013. Sand transport beneath waves: the role of progressive wave streaming and other free surface effects. J. Geophys. Res. Earth Surf. 118, 122–139. https://doi.org/10.1029/2012JF002427.

Lesser, G.R., Roelvink, J.A., Van Kester, J.A.T.M., Stelling, G.S., 2004. Development and validation of a three-dimensional morphological model. Coast. Eng. 51, 883–915. https://doi.org/10.1016/j.coastaleng.2004.07.014.

Masselink, G., Ruju, A., Conley, D., Turner, I., Ruessink, G., Matias, A., Thompson, C., Castelle, B., Puleo, J., Citerone, V., Wolters, G., 2016. Large-scale barrier dynamics experiment II (BARDEX II): experimental design, instrumentation, test program, and data set. Coast. Eng. 113, 3–18. https://doi.org/10.1016/j.coastaleng.2015.07.009.

Nederhoff, C.M., Kees), 2014. Modelling the effects of hard structures on dune erosion and overwash. In: Hindcasting the Impact of Hurricane Sandy on New Jersey with XBeach. M.Sc. Thesis, Delft University of Technology.

O'Donoghue, T., Wright, S., 2004. Flow tunnel measurements of velocities and sand flux in oscillatory sheet flow for well-sorted and graded sands. Coast. Eng. 51, 1163–1184. https://doi.org/10.1016/j.coastaleng.2004.08.001.

Passeri, D.L., Long, J.W., Plant, N.G., Bilskie, M.V., Hagen, S.C., 2018. The influence of bed friction variability due to land cover on storm-driven barrier island morphodynamics. Coast. Eng. 132, 82–94. https://doi.org/10.1016/j.coastaleng.2017.11.005.

Pender, D., Karunarathna, H., 2013. A statistical-process based approach for modelling beach profile variability. Coast. Eng. 81, 19–29. https://doi.org/10.1016/j.coastaleng.2013.06.006.

Rafati, Y., Hsu, T.-J., Cheng, Z., Yu, X., Calantoni, J., 2020. Armoring and exposure effects on the wave-driven sediment transport. Continent. Shelf Res. 211 https://doi.org/10.1016/j.csr.2020.104291.

Ranasinghe, R., Swinkels, C., Luijendijk, A., Roelvink, D., Bosboom, J., Stive, M., Walstra, D.J., 2011. Morphodynamic upscaling with the MORFAC approach: dependencies and sensitivities. Coast. Eng. 58, 806–811. https://doi.org/10.1016/j.coastaleng.2011.03.010.

Reniers, A.J.H.M., Roelvink, J.A., Thornton, E.B., 2004. Morphodynamic modeling of an embayed beach under wave group forcing. J. Geophys. Res. Ocean. 109, 1–22. https://doi.org/10.1029/2002jc001586.

Ribas, F., de Swart, H.E., Calvete, D., Falqués, A., 2011. Modeling waves, currents and sandbars on natural beaches: the effect of surface rollers. J. Mar. Syst. 88, 90–101. https://doi.org/10.1016/j.jmarsys.2011.02.016.

Ribberink, J.S., Al-Salem, A.A., 1994. Sediment transport in oscillatory boundary layers in cases of rippled beds and sheet flow. J. Geophys. Res. Ocean. 99, 12707–12727. https://doi.org/10.1029/94JC00380.

Rienecker, M.M., Fenton, J.D., 1981. A fourier approximation method for steady water waves. J. Fluid Mech. 104, 119–137. https://doi.org/10.1017/S0022112081002851.

Rocha, M.V.L., Michallet, H., Silva, P.A., 2017. Improving the parameterization of wave nonlinearities – the importance of wave steepness, spectral bandwidth and beach slope. Coast. Eng. 121, 77–89. https://doi.org/10.1016/j.coastaleng.2016.11.012.

Roelvink, D., Costas, S., 2019. Coupling nearshore and aeolian processes: XBeach and duna process-based models. Environ. Model. Software 115, 98–112. https://doi.org/10.1016/j.envsoft.2019.02.010.

Roelvink, D., Costas, S., 2017. Beach berms as an essential link between subaqueous and subaerial beach/dune profiles. Geotemas 17, 79–82.

Roelvink, D., McCall, R., Mehvar, S., Nederhoff, K., Dastgheib, A., 2018. Improving predictions of swash dynamics in XBeach: the role of groupiness and incident-band runup. Coast. Eng. 134, 103–123. https://doi.org/10.1016/j.coastaleng.2017.07.004.

Roelvink, D., Reniers, A., Van Dongeren, A., Van Thiel de Vries, J., McCall, R., Lescinski, J., 2009. Modelling storm impacts on beaches, dunes and barrier islands. Coast. Eng. 56, 1133–1152. https://doi.org/10.1016/j.coastaleng.2009.08.006.

Ruessink, B.G., Blenkinsopp, C., Brinkkemper, J.A., Castelle, B., Dubarbier, B., Grasso, F., Puleo, J.A., Lanckriet, T., 2016. Sandbar and beach-face evolution on a prototype coarse sandy barrier. Coast. Eng. 113, 19–32. https://doi.org/10.1016/j.coastaleng.2015.11.005.

Ruessink, B.G., Ramaekers, G., Van Rijn, L.C., 2012. On the parameterization of the free-stream non-linear wave orbital motion in nearshore morphodynamic models. Coast. Eng. 65, 56–63. https://doi.org/10.1016/j.coastaleng.2012.03.006.

Schambach, L., Grilli, A.R., Grilli, S.T., Hashemi, M.R., King, J.W., 2018. Assessing the impact of extreme storms on barrier beaches along the Atlantic coastline: application to the southern Rhode Island coast. Coast. Eng. 133, 26–42. https://doi.org/10.1016/j.coastaleng.2017.12.004.

Schwartz, R.K., Birkemeier, W.A., 2004. Sedimentology and morphodynamics of a barrier island shoreface related to engineering concerns, Outer Banks, NC, USA. Mar. Geol. 211, 215–255. https://doi.org/10.1016/j.margeo.2004.05.020.

Schweiger, C., Kaehler, C., Koldrack, N., Schuettrumpf, H., 2020. Spatial and temporal evaluation of storm-induced erosion modelling based on a two-dimensional field case including an artificial unvegetated research dune. Coast. Eng. 161 https://doi.org/10.1016/j.coastaleng.2020.103752.

Shi, F., Kirby, J.T., Harris, J.C., Geiman, J.D., Grilli, S.T., 2012. A high-order adaptive time-stepping TVD solver for Boussinesq modeling of breaking waves and coastal inundation. Ocean Model. 43 (44), 36–51. https://doi.org/10.1016/j.ocemod.2011.12.004.

Simmons, J.A., Splinter, K.D., Harley, M.D., Turner, I.L., 2019. Calibration data requirements for modelling subaerial beach storm erosion. Coast. Eng. 152 https://doi.org/10.1016/j.coastaleng.2019.103507.

Splinter, K.D., Palmsten, M.L., 2012. Modeling dune response to an east coast low. Mar. Geol. 329–331, 46–57. https://doi.org/10.1016/j.margeo.2012.09.005.

Svendsen, I.A., 1984a. Mass flux and undertow in a surf zone. Coast. Eng. 8, 347–365. https://doi.org/10.1016/0378-3839(84)90030-9.

Svendsen, I.A., 1984b. Wave heights and set-up in a surf zone. Coast. Eng. 8, 303–329. https://doi.org/10.1016/0378-3839(84)90028-0.

Thornton, E.B., Humiston, R.T., Birkemeier, W., 1996. Bar/trough generation on a natural beach. J. Geophys. Res. C Oceans 101, 12097–12110. https://doi.org/10.1029/96JC00209.

Thornton, E.B., Kim, C.S., 1993. Longshore current and wave height modulation at tidal frequency inside the surf zone. J. Geophys. Res. 98, 16509–16519. https://doi.org/10.1029/93jc01440.

Van der A, D.A., O'Donoghue, T., Ribberink, J.S., 2010. Measurements of sheet flow transport in acceleration-skewed oscillatory flow and comparison with practical formulations. Coast. Eng. 57, 331–342. https://doi.org/10.1016/j.coastaleng.2009.11.006.

Van der A, D.A., Ribberink, J.S., Van der Werf, J.J., O'Donoghue, T., Buijsrogge, R.H., Kranenburg, W.M., 2013. Practical sand transport formula for non-breaking waves and currents. Coast. Eng. 76, 26–42. https://doi.org/10.1016/j.coastaleng.2013.01.007.

Van der Lugt, M.A., Quataert, E., Van Dongeren, A., Van Ormondt, M., Sherwood, C.R., 2019. Morphodynamic modeling of the response of two barrier islands to Atlantic hurricane forcing. Estuar. Coast Shelf Sci. 229 https://doi.org/10.1016/j.ecss.2019.106404.

Van der Zanden, J., van der A, D.A., Hurther, D., Caceres, I., O'Donoghue, T., Hulscher, S.J.M.H., Ribberink, J.S., 2017. Bedload and suspended load contributions to breaker bar morphodynamics. Coast. Eng. 129, 74–92. https://doi.org/10.1016/j.coastaleng.2017.09.005.

Van Rijn, L.C., 2007a. Unified view of sediment transport by currents and waves. I: initiation of motion, bed roughness, and bed-load transport. J. Hydraul. Eng. 133, 649–667. https://doi.org/10.1061/(ASCE)0733-9429(2007)133:6(649).

Van Rijn, L.C., 2007b. Unified view of sediment transport by currents and waves. II: suspended transport. J. Hydraul. Eng. 133, 668–689. https://doi.org/10.1061/(ASCE)0733-9429(2007)133:6(668).

Van Rijn, L.C., Wasltra, D.J.R., Grasmeijer, B., Sutherland, J., Pan, S., Sierra, J.P., 2003. The predictability of cross-shore bed evolution of sandy beaches at the time scale of storms and seasons using process-based profile models. Coast. Eng. 47, 295–327. https://doi.org/10.1016/S0378-3839(02)00120-5.

Van Thiel De Vries, J.S.M., 2009. Dune Erosion during Storm Surges. Ph.D. Thesis, Delft University of Technology.

Vousdoukas, M.I., Ferreira, O., Almeida, Luis P., Pacheco, A., 2012. Toward reliable storm-hazard forecasts: XBeach calibration and its potential application in an operational early-warning system. Ocean Dynam. 62, 1001–1015. https://doi.org/10.1007/s10236-012-0544-6.

Walstra, D.J.R., Mocke, G.P., Smit, F., 1996. Roller contributions as inferred from inverse modelling techniques. In: Coastal Engineering Proceedings, pp. 1205–1218. https://doi.org/10.1061/9780784402429.094. Orlando, Florida, USA.

Warner, J.C., Armstrong, B., He, R., Zambon, J.B., 2010. Development of a coupled ocean-atmosphere-wave-sediment transport (COAWST) modeling system. Ocean Model. 35, 230–244. https://doi.org/10.1016/j.ocemod.2010.07.010.

Wenneker, I., van Dongeren, A., Lescinski, J., Roelvink, D., Borsboom, M., 2011. A Boussinesq-type wave driver for a morphodynamical model to predict short-term morphology. Coast. Eng. 58, 66–84. https://doi.org/10.1016/j.coastaleng.2010.08.007.

Zijlema, M., Stelling, G., Smit, P., 2011. SWASH: an operational public domain code for simulating wave fields and rapidly varied flows in coastal waters. Coast. Eng. 58, 992–1012. https://doi.org/10.1016/j.coastaleng.2011.05.015.